International Journal of Multiphase Flow 178 (2024) 104882

Contents lists available at ScienceDirect

International Journal of Multiphase Flow

journal homepage: www.elsevier.com/locate/ijmulflow

Solid–fluid force modeling: Insights from comparing a reduced order model for a pair of particles with resolved CFD-DEM

Lucka Barbeau [a], Stéphane Étienne [b], Cédric Béguin [b], Bruno Blais [a,*]

[a] CHAOS Laboratory, Department of Chemical Engineering, École Polytechique de Montréal, PO Box 6079, Stn Centre-Ville, Montréal, QC, Canada H3C 3A7
[b] Department of Mechanical Engineering, École Polytechique de Montréal, PO Box 6079, Stn Centre-Ville, Montréal, QC, Canada H3C 3A7

ARTICLE INFO

Keywords:
Pair-wise particle interaction
Reduced order modeling
Immersed boundary
Navier–Stokes incompressible flow
Computational fluid dynamics with the discrete element method (CFD-DEM)

ABSTRACT

Solid–fluid force models are essential to efficiently model multiple industrial apparatuses such as fluidized beds, spouted beds, and slurry transport. They are generally built using strong hypotheses (e.g. fully developed flow and no relative motion between particles) that affect their accuracy. We study the effect of these hypotheses on particle dynamics using the sedimentation of a pair of particles. We develop new induced drag, lift and torque models for pairs of particles based on an artificial neural network (ANN) regression. The fluid force model covers a range of Reynolds numbers of 0.1 to 100 and particle centroid distance of up to 9 particle diameters. The ANN model uses 3475 computational fluid dynamics (CFD) simulation results as the training data set. Using this fluid force model, we develop a reduced-order model (ROM), which includes the virtual mass force, the Meshchersky force, the history force, the lubrication force, and the Magnus force. Using the results of a resolved computational fluid dynamics coupled with a discrete element method (CFD-DEM) model as a reference, we analyze the discrepancies between the ROM and CFD-DEM results for a series of sedimentation cases that cover particle Archimedes number from 20 to 2930 and particle to fluid density ratio of 1.5 to 1000. The errors primarily stem from particle history interactions that are not accounted for by the fully developed flow hypothesis. The importance of this effect on the dynamic of two particles is isolated and it is shown that it is more pronounced in cases with a lower particle-to-fluid density ratio (such as solid–liquid cases). This work underscores the need for more research on these effects to increase the precision of solid–fluid force models for small particle-to-fluid density ratios (1.5).

1. Introduction

Solid–fluid force closure models are essential to simulate large-scale systems in feasible computational time. They are required to model fluidized beds, slurry transport spouted beds, and other industrial operations. These operations are commonly simulated using unresolved computational fluid dynamics simulation (CFD) coupled with a discrete element method (DEM) (unresolved CFD-DEM) (Golshan et al., 2020) or using two-fluid models. Both approaches require solid–fluid force models to couple the momentum of the solid and fluid phases. The solid–fluid force models must account for multiple particles within a compact cluster and the Reynolds number to accurately predict the forces acting on the particles and the fluid. The presence of other particles is often only statistically considered through the volume fraction occupied by the fluid (void fraction) (Ergun, 1952; Rong et al., 2013; Di Felice, 1994). Some models also consider the void fraction gradient to consider the spatial arrangement of the particles, which induces lift (Li et al., 2017; Su and Zhao, 2017). In unresolved CFD-DEM, recent models further improve the accuracy of the solid–fluid force by directly considering the disposition of neighboring particles (Akiki et al., 2017; Cheng and Wachs, 2023; Seyed-Ahmadi and Wachs, 2020). The fluid interaction between particles is not limited to modification of the solid–fluid force; it also generates torques on the particle that are highly dependant on the particle arrangement (Cheng and Wachs, 2023). Force models are based on cases where the particles are static relative to each other, and the flow is fully developed. In natural systems, particles are in motion relative to each other, and various transient effects generate additional forces and torques that may affect the predictive capacity of the simulation (Marchelli and Di Felice, 2023; Kriebitzsch et al., 2013).

Even in the relatively simple case of two identical particles, the solid–fluid force applied to one of them is a function of 35 variables and has a dimensionality of three (time, length, mass), which implies, by the Buckingham-Pi theorems, 32 dimensionless numbers. Table 1 presents the list of these variables if a pair of particles is moving in a fluid

* Corresponding author.
E-mail address: bruno.blais@polymtl.com (B. Blais).

https://doi.org/10.1016/j.ijmultiphaseflow.2024.104882
Received 18 October 2023; Received in revised form 7 May 2024; Accepted 25 May 2024
Available online 10 June 2024
0301-9322/© 2024 The Author(s). Published by Elsevier Ltd. This is an open access article under the CC BY license (http://creativecommons.org/licenses/by/4.0/).

that is motionless away from the particles. Some phenomena associated with these variables lead to force with specific names such as the drag force (Clift et al., 2005), the virtual mass force (Béguin et al., 2016), the Meshchersky force (Zoghlami et al., 2019), the history force (Mei and Adrian, 1992), the lubrication force (O'Neill and Majumdar, 1970), the Saffman force (Loth, 2008), and the Magnus force (Loth, 2008). The effect of the relative position of particles within a pair on the solid–fluid force has been studied extensively (Smoluchowski, 1911; Happel and Brenner, 1983; Eveson et al., 1959; Chen and Lu, 1999; Chen and Wu, 2000; Prahl et al., 2007). The work of Prahl et al. (2007) gives an extensive characterization of the effect of the relative position on the solid–fluid force applied on a pair of particles at moderate Reynolds numbers (50–200). However, their work does not present a closed-form correlation that encompasses their results. For Stokes flow, Faxén introduced a rigorous way to assess the forces on a set of particles (Faxen, 1923). Gatignol improved his work by considering the non-uniformity of the flow around the particles (Gatignol, 1983). This rigorous approach was recently applied to the dynamics case of two particles by Ardekani and Rangel (2006). Outside of Stokes' flow, dynamic models require the combination of multiple force correlations. Among others, Nijssen et al. (2020) proposed a combination of correlations to generate a solid–fluid force model that is valid outside the Stokes regime. However, these correlations are built on hypotheses that cannot always be respected if the particles are in motion (e.g., fully developed flow and no relative particles' motion). The potential consequences of not fully adhering to them in the dynamics of a swarm of particles remain unknown.

This study explores the impact of the fully developed flow hypothesis on the fluid–solid force model, specifically examining the dynamics of a pair of particles. To address this, we introduce a novel correlation derived from an artificial neural network (ANN) regression designed to model the drag force, induced lift force, and induced torque experienced by a pair of particles. This model incorporates the relative positions of the particles (both distance and angular orientation with respect to the flow) and the Reynolds number as inputs. The correlation encompasses Reynolds numbers ranging from 0.1 to 100 and particle centroid distances up to nine particle diameters. The training dataset for the ANN is generated using Lethe, an open-source CFD software (Blais et al., 2020; Barbeau et al., 2022), following the methodology proposed by Bibeau et al. (2023). The minimal error in the correlations allows for a detailed analysis of the errors arising from disregarding transient effects. Subsequently, this correlation is incorporated into a dynamical model (ROM) that simulates both angular and translational positions and velocities of particles, accounting for various solid–fluid forces such as the virtual mass force, history force, and lubrication forces. This model has been validated through sedimentation experiments with a single particle. Using this ROM, we assess the predictive capabilities of models that only use two parameters (Reynolds number and relative particle position) to define the drag and lift forces and the induced torque between particles. Results for the sedimentation of two particles are compared to results obtained using particle-resolved CFD-DEM conducted with Barbeau et al. (2024). The sedimentation cases cover Archimedes' numbers from 20 to 2930 and a particle-to-fluid density ratio of 1.5 to 1000. This analysis demonstrates that the ROM accurately predicts particle dynamics at high particle-to-fluid density ratios. It also highlights some discrepancies at lower density ratios. These discrepancies are linked to the fully developed flow hypothesis and the interaction between the particles during the acceleration of the fluid. Additionally, the effect of rotation on the particles' dynamics is measured using resolved CFD-DEM. The rotation impacts particle dispersion and affects more cases with high-density ratios and higher Archimedes numbers. Finally, the effect of considering the relative velocity between the particles in the force model using a quasistatic hypothesis is analyzed. This work underlines limitations in the capacity of fluid-force models to predict the transient behavior of liquid–solid systems.

2. ANN regression of a particle pair fluid force interactions

Currently, no correlation exists to calculate the induced drag, lift forces, and torque on a particle due to the presence of another particle in its vicinity. To address this, an ANN is employed to perform a regression analysis on a large dataset of CFD simulation results, which include the drag, lift, and torque acting on a pair of particles. The resulting correlation determines the forces and torque exerted on the particles under several assumptions: the particles are fixed within an undisturbed flow, the flow is fully developed without three-dimensional instability (all interactions occur within the plane defined by $\boldsymbol{v} \times \boldsymbol{r}$), no buoyancy force is present, and the particles exhibit zero angular velocity. These assumptions reduce the 32 dimensionless numbers, detailed in Table 1, to a manageable system of four dimensionless numbers per dependent variable.

Table 2 outlines the three dependent variables — the two components of force (drag and induced lift) and the induced torque — as well as the six independent variables. This arrangement produces three dependent dimensionless numbers: drag coefficient (Cd), lift coefficient (Cl), and torque coefficient (Ct), each dependent on three independent dimensionless numbers: Re, r^*, and θ. Due to the system's symmetry, θ is defined within the range $[0, \pi]$.

2.1. Creation of the data set

The data set is generated using the sharp interface immersed boundary finite element solver implemented in Lethe (Barbeau et al., 2022; Blais et al., 2020), a high-order CFD simulation tool that utilizes the deal.ii finite element library (Arndt et al., 2022). This sharp interface immersed boundary facilitates the imposition of the no-slip boundary condition directly on the surface of a particle, eliminating the need for meshing while maintaining the accuracy of the underlying finite element scheme. Previous results using the same simulation tool have demonstrated that using elements of type Q2-Q1 (quadratic hexahedral elements for the velocity field and linear hexahedral elements for the pressure field) significantly reduces the computational time required to achieve hydrodynamic force calculations on a particle with accuracy within 1% (Daunais et al., 2023; Barbeau et al., 2024). These studies also explore the effect of domain size on drag force, recommending that boundaries be at least 30 particle diameters from the nearest particle. For this study, a rectangular domain of $180 \times 90 \times 90(d_p)$ was chosen, centering the first particle at $(54, 45, 45)$ and allowing the second particle to move within a nine-particle-diameter sphere around it. This setup ensures the nearest wall remains at least 30 particle diameters away. The data set spans Reynolds numbers $Re \in [0.1, 100]$, centroid distances $r^* \in [1, 9]$, and angles $\theta \in [0, \pi]$. It consists of two parts: structured sampling as detailed in Table 3, and Latin hypercube sampling (McKay et al., 2000), which together provide 2475 and 1000 data points respectively, via logarithmic spacing for Re and r^*. The data set includes 3475 data points, substantiating its size and guaranteeing the model's independence from specific data set characteristics.

The mesh consists of a coarse grid with an element size of $3.75d_p$. This coarse grid includes two initial refinement zones around the particles. Initially, a rectangular refinement box envelops the particles with a maximum element size of $\Delta x = 0.1172d_p$ (zone Z1), followed by a spherical zone around each particle where the mesh is refined to the smallest element size allowed (zone Z2). Fig. 1 presents a sectional view of the domain on the particle plane, illustrating the different refinement zones (Z1 and Z2) and their dimensions. Additionally, 10% of the mesh undergoes further refinement using the Kelly error estimator, based on the velocity field, to refine the recirculation zone in the wake of the particles (Kelly et al., 1983). This additional refinement process is repeated four times.

Cases with the two particles positioned side by side at a Reynolds number of 100 are utilized for the mesh convergence analysis. Two scenarios are examined: particles in contact ($r^* = 1$) and particles

Table 1
Without any hypothesis on the initial conditions, we obtained a system with 35 variables to express the total solid–fluid force on one particle.

Variable	Name	SI units	Number of components	Dimensions
$\boldsymbol{f}$	Particle 1 solid–fluid force	$\mathrm{kg\,m\,s^{-2}}$	3	$\mathrm{MLT^{-2}}$
d_p	Particles diameter	m	1	L
ρ_f	Fluid density	$\mathrm{kg\,m^{-3}}$	1	$\mathrm{ML^{-3}}$
$\lVert g \rVert$	Gravity norm	$\mathrm{m\,s^{-2}}$	1	$\mathrm{LT^{-2}}$
μ	Dynamic viscosity	$\mathrm{kg\,m^{-1}\,s^{-1}}$	1	$\mathrm{ML^{-1}T^{-1}}$
$\boldsymbol{r}$	Particles relative position vector	m	3	L
$\boldsymbol{v}_1$	Particle 1 velocity	$\mathrm{m\,s^{-1}}$	3	$\mathrm{LT^{-1}}$
$\boldsymbol{v}_2$	Particle 2 velocity	$\mathrm{m\,s^{-1}}$	3	$\mathrm{LT^{-1}}$
$\frac{d\boldsymbol{v}_1}{dt}$	Particle 1 acceleration	$\mathrm{m\,s^{-2}}$	3	$\mathrm{LT^{-2}}$
$\frac{d\boldsymbol{v}_2}{dt}$	Particle 2 acceleration	$\mathrm{m\,s^{-2}}$	3	$\mathrm{LT^{-2}}$
$\boldsymbol{\omega}_1$	Particle 1 angular velocity	$\mathrm{s^{-1}}$	3	$\mathrm{T^{-1}}$
$\boldsymbol{\omega}_2$	Particle 2 angular velocity	$\mathrm{s^{-1}}$	3	$\mathrm{T^{-1}}$
$\frac{d\boldsymbol{\omega}_1}{dt}$	Particle 1 angular acceleration	$\mathrm{s^{-2}}$	3	$\mathrm{T^{-2}}$
$\frac{d\boldsymbol{\omega}_2}{dt}$	Particle 2 angular acceleration	$\mathrm{s^{-2}}$	3	$\mathrm{T^{-2}}$
t	Time	s	1	T

Table 2
Assuming that particles maintain the same constant velocity, that the flow is fully developed, and that there are no three-dimensional instability has developed (all interactions occur within the plane defined by $\boldsymbol{v}\times\boldsymbol{r}$), coupled with the absence of buoyancy force and zero angular velocity for the particle, the system of variables in Table 1 is simplified. These conditions reduce the system to nine essential variables required to express the forces and torque acting on a particle.

Variables	Number of components	Dimensions	Associated dimensionless numbers
$\boldsymbol{f}$	2	$\mathrm{MLT^{-2}}$	$Cd = \frac{-8F_{\lVert v}}{\rho_f d_p^2 \pi \lVert \boldsymbol{v} \rVert^2}$, $Cl = \frac{8F_{\perp \boldsymbol{v}}}{\rho_f d_p^2 \pi \lVert \boldsymbol{v} \rVert^2}$
$\boldsymbol{T}$	1	$\mathrm{ML^2T^{-2}}$	$Ct = \frac{16\lVert \boldsymbol{T} \rVert}{\rho_f d_p^3 \pi \lVert \boldsymbol{v} \rVert^2}$
d_p	1	L	repeating variable
ρ_f	1	$\mathrm{ML^{-3}}$	repeating variable
μ	1	$\mathrm{ML^{-1}T^{-1}}$	$Re = \frac{\lVert \boldsymbol{v} \rVert d_p \rho_f}{\mu}$
$\boldsymbol{r}$	2	L	$r^* = \frac{\lVert \boldsymbol{r} \rVert}{d_p}$, $\theta = acos\left(\frac{-\boldsymbol{v}\cdot\boldsymbol{r}}{\lVert \boldsymbol{v} \rVert \lVert \boldsymbol{r} \rVert}\right)$
$\boldsymbol{v} = \boldsymbol{v}_1 = \boldsymbol{v}_2$	1	$\mathrm{LT^{-1}}$	repeating variable

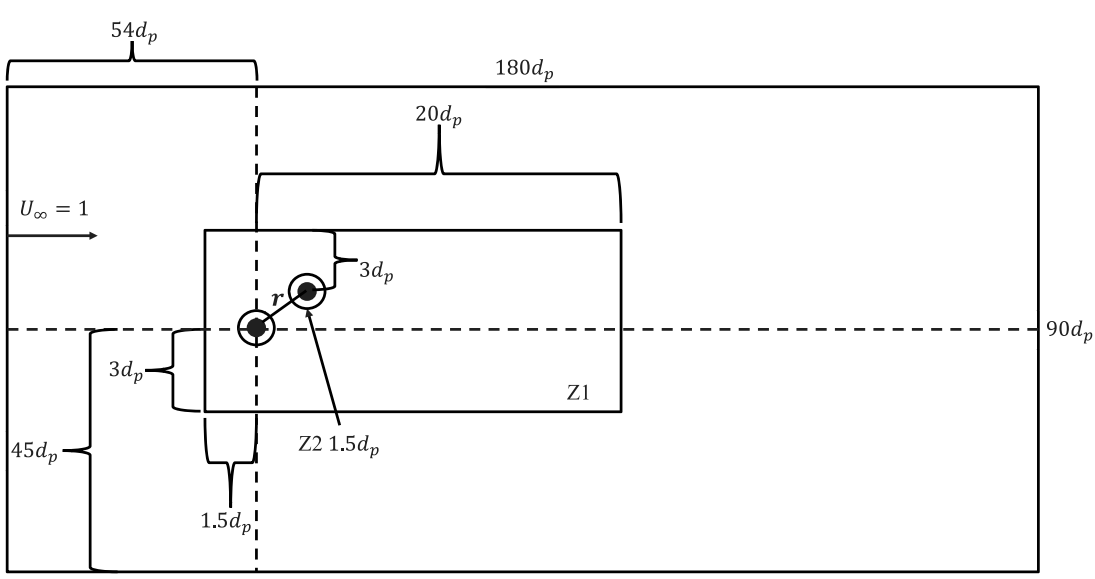

Fig. 1. Representation of the simulation domain and the two refinement zones (Z1 and Z2) around the particles. The refinement zone Z1 guarantees a minimal element size of $0.1172d_p$, and the refinement zone Z2 guarantees the minimal element size allowed.

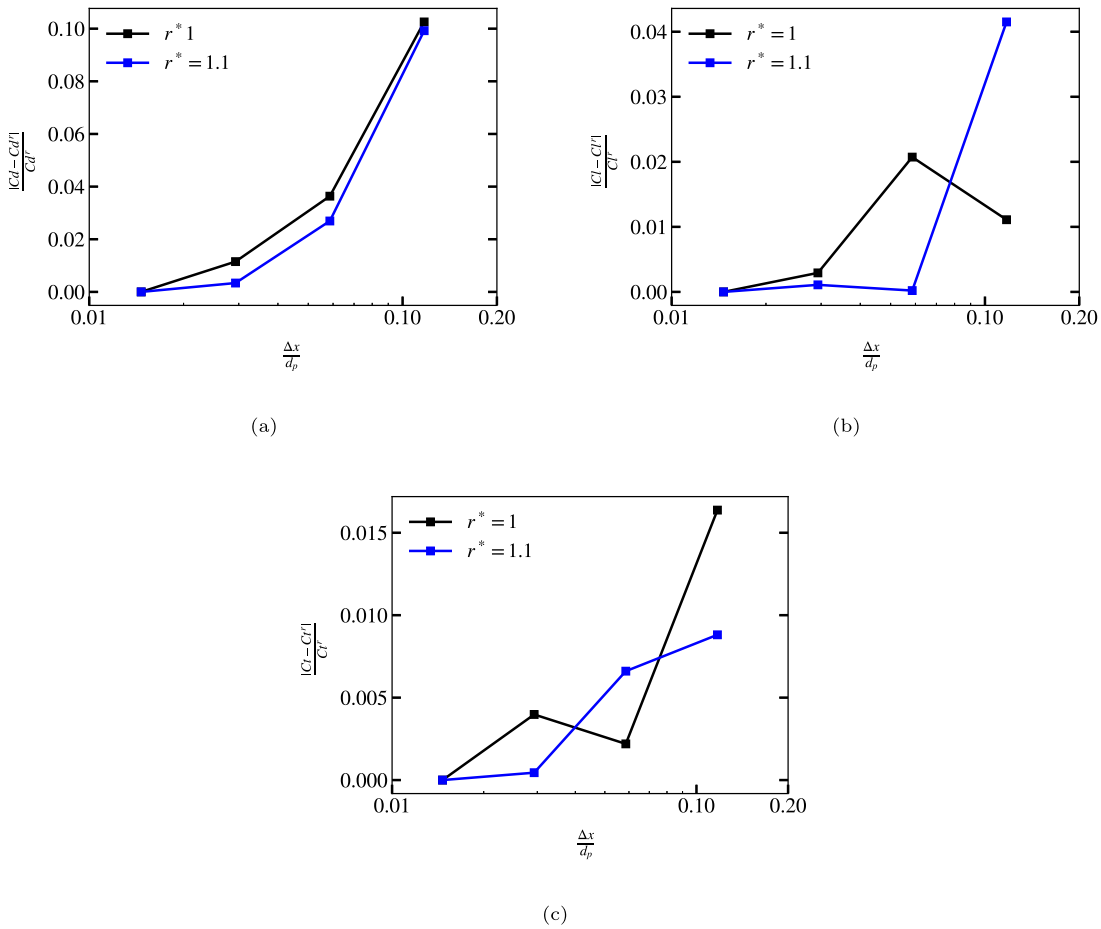

Fig. 2. Mesh sensitivity analysis of the relative error on Cd, Cl, and Ct. The variables reported with ^{r} are evaluated at the smallest ($\frac{\Delta x}{d_p} = \frac{15}{1024}$). The Δx reported is the smallest space discretization in a given discretization.

Table 3
Structured sampling of the three independent dimensionless numbers used to analyze the modification of the solid–fluid force as a function of the Reynolds number and the relative particle position. All combinations of these three variables are sampled for a total of 2475 data points.

Variables	Sampled value
r^*	$1 + 2^n \forall n \in \{-\infty, -4, -3, -2.5, -2, -1.5, -1, -0.5, 0, 0.5, 1, 1.5, 2, 2.5, 3\}$
Re	0.1, 1, 54, 10, 100
θ	$\frac{n\pi}{32} \forall n \in [0, 32] \mid n \in \mathbb{N}$

separated by $\frac{1}{10}$ of the particle diameter ($r^* = 1.1$). The convergence of these cases was representative of similar scenarios with varying angles between the particles and the flow direction. Fig. 2 displays the relative convergence achieved for all three dependent dimensionless numbers based on the smallest element of the mesh. A mesh with a discretization size of $\Delta x = \frac{15}{512} d_p$ yields satisfactory results, within 1% of those obtained using the finest mesh, and is therefore chosen for the simulations.

2.2. Definition of the ANN training parameters

An ANN is trained for each dependent dimensionless number (Cd, Cl, Ct) following the procedure described by Bibeau et al. (2023). The ANN utilizes the TensorFlow library (Abadi et al., 2015) with Adamax as the optimizer (Géron, 2022). Network initialization is performed using the Glorot uniform distribution (Glorot and Bengio, 2010), and the mean squared error is employed as the cost function. Prior to training, the dataset is normalized relative to Cd_0 to mitigate issues arising from varied coefficient scaling across different Reynolds numbers. The coefficients ($\frac{Cd}{Cd_0}, \frac{Cl}{Cd_0}, \frac{Ct}{Cd_0}$) are subsequently scaled between 0 and 1 using a MinMax approach. Each predicted variable is modeled using a separate network, though all share the same architecture. An exhaustive grid search with cross-validation is conducted to determine the optimal number of layers and neurons per layer. The dataset, as described in Section 2.1, is divided into three parts: training, validation, and testing datasets. Seventy percent of the data is utilized for training and cross-validation, while the remaining 30% forms the untrained testing set. Cross-validation is used to monitor the training of the ANN and ensure that there is no overfitting. The process results in an ANN configured with 75 neurons per layer across six layers, employing the hyperbolic tangent as the activation function and trained over 30,000 epochs. Following this, the network undergoes a final training phase without cross-validation to establish the definitive correlation for each dimensionless number.

2.3. ANN validation

To validate the ANN correlation, the results of the ANN for the testing dataset are plotted against the simulation results in Fig. 3. All ANN predictions agree with the simulation results ($R^2 > 0.999$), and the relative root mean square error on the test dataset is under 2% for all three correlations obtained. These results are sufficiently accurate for use in the ROM.

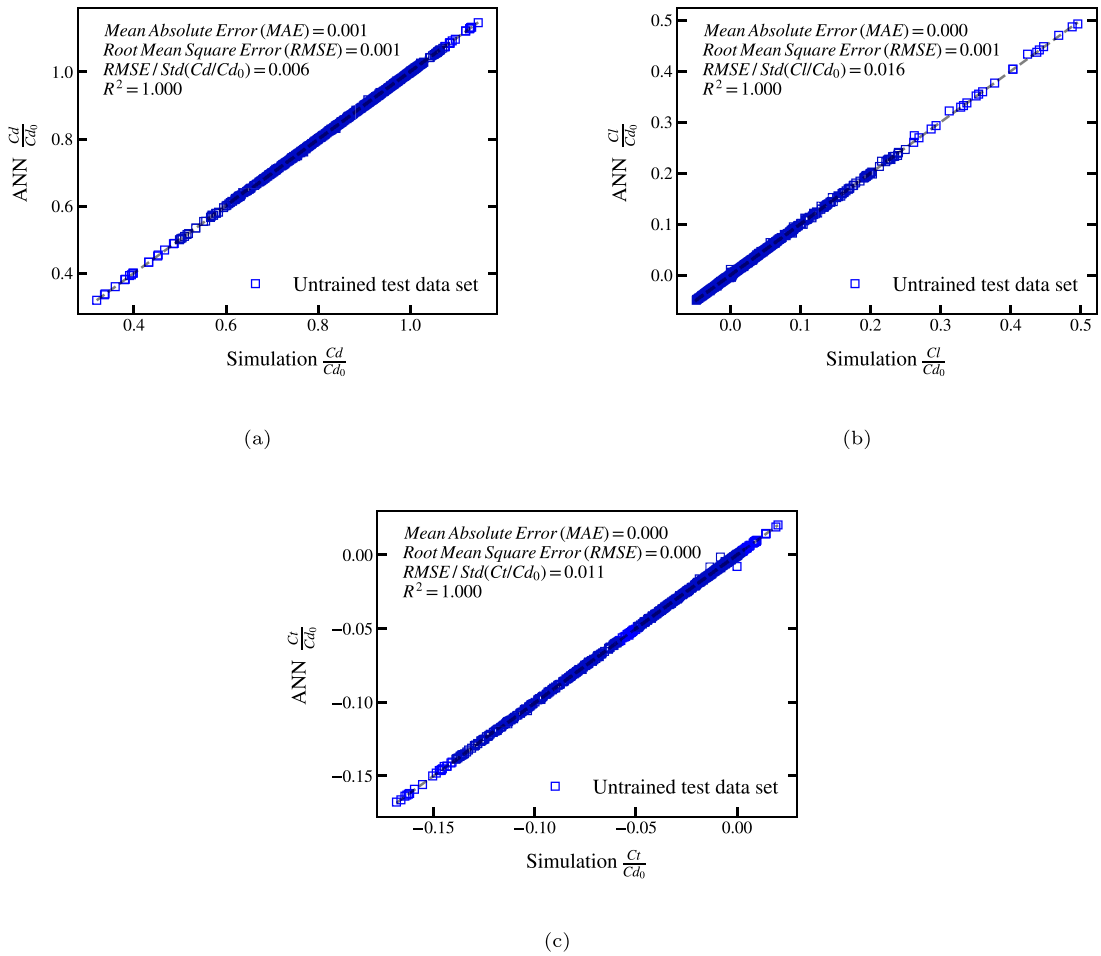

Fig. 3. Parity plot of the Cd, Cl, and Ct ANN correlations with the testing data set (30%of the data set) and the untrained data at Reynolds 54. All three correlations agree well with the simulation results ($R^2 > 0.999$).

2.4. Validation of the model

The simulation results and ANN correlation are compared to various results found in the literature. The results displayed are normalized by the drag coefficient of a single particle (Cd_0) to ensure consistency with findings reported in the literature. Cd_0 is defined by the correlation of Clift et al. (2005):

$$Cd_0 = \begin{cases} \frac{24}{\mathrm{Re}}\left(1 + 0.1315\mathrm{Re}^{0.82-0.05log_{10}(\mathrm{Re})}\right), & \text{if Re} \leq 20 \\ \frac{24}{\mathrm{Re}}\left(1 + 0.1935\mathrm{Re}^{0.6305}\right), & \text{otherwise} \end{cases} \tag{1}$$

This normalization process also maintains the scale of the dimensionless numbers ($\frac{Cd}{Cd_0}$, $\frac{Cl}{Cd_0}$, $\frac{Ct}{Cd_0}$) across different Reynolds numbers. The results in Fig. 4 show good agreement with the findings reported in the literature for the drag coefficient (Prahl et al., 2007; Chen and Lu, 1999; Chen and Wu, 2000; Liang et al., 1996; Zhu et al., 1994; Jin et al., 2019). Similarly, the results for the lift coefficient, as shown in Fig. 5, align well with those of Prahl et al. (2007). Notably, the results of Prahl et al. (2007) for the lift force were not originally normalized by Cd_0, which has been done here for comparative purposes. These results are deemed sufficiently accurate for use in a solid–fluid force model.

3. Reduced order model

The ROM consists of a set of ordinary differential equations (ODEs). In the sedimentation cases, the undisturbed flow is assumed to be zero. This assumption aligns with considering an infinite control volume for fluid dynamics, ensuring consistency with the control volume used in the pairwise fluid force model described in Section 2. Consequently, the ROM benefits from being interpreted as a change of reference frame compared to the results used to generate the drag force model. The ROM builds on the work of Nijssen et al. (2020) and includes a versatile combination of solid–fluid force models: drag, Magnus lift, Saffman lift, virtual mass, and history forces. In their approach, the lubrication force was adjusted by modifying the particle restitution coefficient. All these force models, except for the Saffman force — due to the undisturbed fluid velocity having zero gradient — are incorporated into the ROM. Additionally, the ROM integrates the Meshchersky force (Zoghlami et al., 2019) and directly applies the lubrication force. The induced lift is incorporated using the ANN model outlined in Section 2. For angular velocity, the ROM considers the inter-particle induced torque defined in Section 2 along with the viscous torque. Furthermore, the ROM accounts for the particle–particle contact force, although it neglects the contact torque. The restitution coefficient is set at 1 for all cases. Table 4 lists the force and torque models employed in the ROM, and Appendix A details the equations for each model. The ODEs describing the particle dynamics are presented as follows:

$$\frac{d\boldsymbol{v}_i}{dt} = \frac{1}{m_i}\left(\sum_{\substack{j=0\\ i\neq j}}^{1}\left(\boldsymbol{f}_{ij}^{c} + \boldsymbol{f}_{ij}^{lub} + \boldsymbol{f}_{ij}^{d} + \boldsymbol{f}_{ij}^{l} + \boldsymbol{f}_{ij}^{v} + \boldsymbol{f}_{ij}^{m}\right) + \boldsymbol{f}_{i}^{h} + \boldsymbol{f}_{i}^{mag} + \boldsymbol{f}_{i}^{b}\right) \tag{2}$$

$$\frac{d\boldsymbol{\omega}_i}{dt} = \frac{1}{I_i}\left(\sum_{\substack{j=0\\ i\neq j}}^{1}\left(\boldsymbol{T}_{ij}^{I} + \boldsymbol{T}_{ij}^{lub}\right) + \boldsymbol{T}_{i}^{v}\right) \tag{3}$$

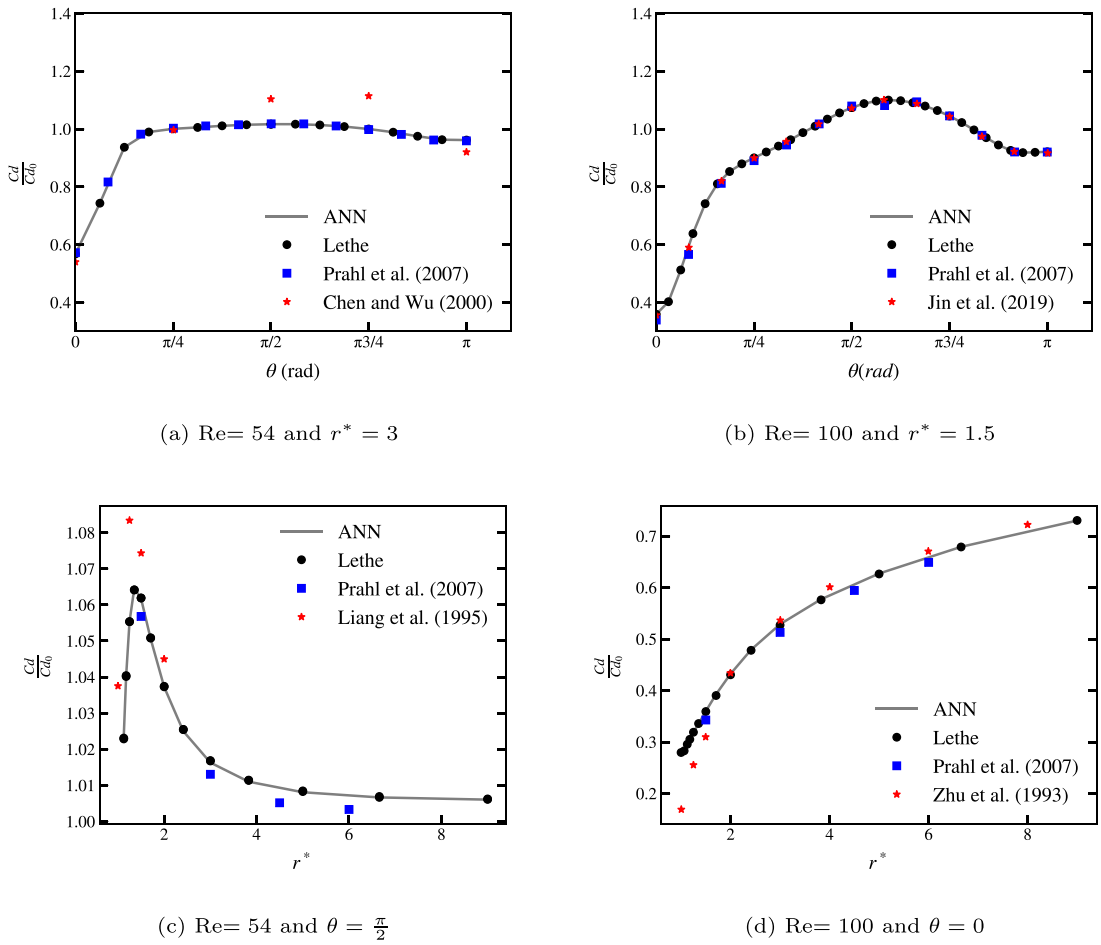

(a) Re= 54 and $r^* = 3$ (b) Re= 100 and $r^* = 1.5$

(c) Re= 54 and $\theta = \frac{\pi}{2}$ (d) Re= 100 and $\theta = 0$

Fig. 4. Comparison of results obtained for the modification of the drag coefficient with various results in the literature (Prahl et al., 2007; Chen and Lu, 1999; Chen and Wu, 2000; Liang et al., 1996; Zhu et al., 1994; Jin et al., 2019).

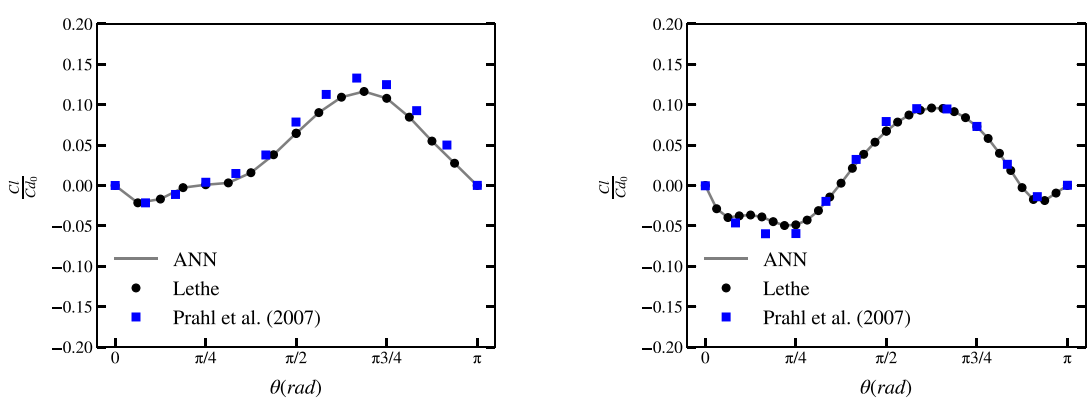

(a) Re= 54 and $r^* = 1.5$ (b) Re= 100 and $r^* = 1.5$

Fig. 5. Comparison of results obtained for the modification of the lift coefficient with the results of Prahl et al. (2007). Note Prahl et al. (2007) results were carried out at a Reynolds number of 50 instead of 54.

Eq. (11) uses a uniform moment of inertia for the particles, which are considered filled spheres made of a single material. We note the absence of a torque associated with the angular acceleration of the particle. This term would encompass the torque necessary to accelerate the boundary layer of the particle. In the context of Stokes flows, this term is well described by Candelier et al. (2023). However, adding the Stokesian term to the ROM significantly increased the model error for moderate Reynolds numbers (Re> 1), and no correlation was found for this term outside of the Stokes regime. Consequently, it is neglected in the present work.

Each particle may have a different velocity in Eqs. (10) and (11). This differs from the hypothesis used to define $\boldsymbol{f}^d$, $\boldsymbol{f}^l$, and $\boldsymbol{T}^I$ (see Section 2). The same issue arises in solid–fluid force models used in unresolved CFD-DEM. It is typically addressed by assuming that all

Table 4
Fluid force and torque models and their sources.

Forces and Torques	References
Drag $\boldsymbol{f}^d$	present work
Induced Lift $\boldsymbol{f}^l$	present work
History $\boldsymbol{f}^h$	Parmar et al. (2018)
Virtual Mass $\boldsymbol{f}^v$	Béguin et al. (2016)
Meshchersky $\boldsymbol{f}^m$	Zoghlami et al. (2019)
Lubrication $\boldsymbol{f}^{lub}$	Cooley and O'neill (1969), O'Neill and Majumdar (1970)
Magnus $\boldsymbol{f}^{mag}$	Loth (2008)
Buoyancy $\boldsymbol{f}^b$	–
Contact $\boldsymbol{f}^c$	Cundall and Strack (1979)
Induced torque $\boldsymbol{T}^I$	present work
Viscous torque $\boldsymbol{T}^v$	Ben Salem and Oesterle (1998)
Contact torque $\boldsymbol{T}^c$	Cundall and Strack (1979)

Table 5
Properties of the fluid for each of the four cases proposed by ten Cate et al. (2002).

Case	Reynolds number	ρ(kg m^{-3})	μ(Pa s)
E1	1.5	970	0.373
E2	4.1	965	0.212
E3	11.6	962	0.113
E4	31.9	960	0.058

neighboring particles move with the same velocity as the particle for which the fluid force is evaluated. The current ROM adopts this strategy, meaning that $\boldsymbol{f}^d$, $\boldsymbol{f}^l$, and $\boldsymbol{T}^I$ applied on particle i are evaluated using the velocity of particle i. Additionally, the lubrication force $\boldsymbol{f}^{lub}$ is included to capture the effect of relative particle velocity. However, the developed model does not account for the influence of particles' relative velocity on the configuration of the wake. This oversight could affect the hydrodynamic forces exerted on the particle in ways not addressed by the existing force model.

The correlation for the virtual mass $\boldsymbol{f}^v$ and the Meshchersky $\boldsymbol{f}^m$ forces also takes into account the presence of the other particle. Both directly consider the relative positions of the particles and their acceleration (see Appendix A for more details).

The implementation of the ROM is performed in Python. The scripts and the ANN force model files are available on a public repository (Barbeau, 2023).

3.1. Validation of the reduced order model

The validation of the particle's acceleration and sedimentation velocity in the ROM is conducted by simulating the sedimentation of a single particle and comparing the results of the ROM with particle-resolved simulations Barbeau et al. (2024). The cases are adapted from the original results of ten Cate et al. (2002) by expanding the simulation domain and preventing particle–wall interactions at low Reynolds numbers.

These validation cases involve four sedimentation scenarios of a single particle ($d_p = 1.5$ cm, $\rho_p = 1120$ kg m^{-3}) within a rectangular box measuring $90 \times 90 \times 90$ cm. The particle centroid is positioned 12.75 cm above the bottom of the container and centered relative to the walls. The velocity and Reynolds number are adjusted by modifying the fluid properties. Table 5 details the properties of the fluid for each case.

An explicit Euler scheme with a time step of 0.0005 s is utilized to integrate the ROM. This time step is sufficiently small to ensure that results are independent of the time step. The results of the validation case are depicted in Fig. 6, demonstrating good overall agreement between the ROM and the simulation results. The observed differences fall within the expected range, attributable to the history model used. For more details on the use of the history model and comparisons with other history force models, refer to Dorgan and Loth (2007).

Given the adequate sedimentation velocity observed, the ROM results are deemed satisfactory for these cases, and the model is considered validated.

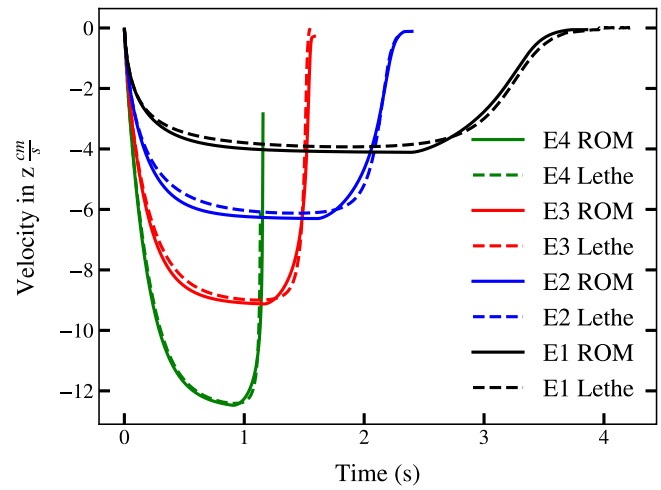

Fig. 6. ROM validation using the modified validation case for a single particle of ten Cate et al. (2002). Results agree with the resolved CFD-DEM results (Barbeau et al., 2024).

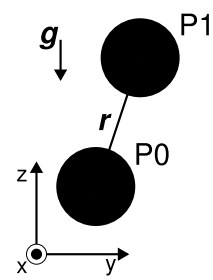

Fig. 7. Standard disposition of the particles pair in a Cartesian frame of reference.

4. Model analysis

Using the ROM, the sedimentation of two particles is analyzed. The set of parameters that define the initial conditions of the pair of particles — assuming both are identical and initially at rest — is determined by four dimensionless numbers. These dimensionless numbers are detailed in Table 6.

The ROM results are analyzed using 12 sedimentation cases described in Table 7. The cases involve two different initial particle dispositions, three Archimedes numbers, and two particle-to-fluid density ratios. The combinations of r^* and θ create two distinct behaviors. Specifically, the configuration ($r^* = 1.5$, $\theta = \frac{\pi}{2}$) causes the particles to strongly repel each other until their interaction becomes negligible as they move apart. Conversely, the configuration ($r^* = 2.06$, $\theta = 0.245$) leads to drafting, kissing, and tumbling (DKT) interactions between the particles. The selected Archimedes (Ar) numbers (20, 319, 2930) correspond to terminal Reynolds numbers for a single particle of (1, 10, 50). The ρ^* values of 1.5 and 1000 are chosen to simulate solid–liquid and solid–gas interactions, respectively. Fig. 7 illustrates the relative positions of the particles in the Cartesian frame.

All interactions occur in the Y-Z plane for the cases considered since these cases do not generate 3-dimensional instability. The typical trajectory of the particles in the Y-Z plane for both initial dispositions of the particles is presented in Fig. 8.

The simulations of these cases in the resolved CFD-DEM module of Lethe utilize Q2-Q1 elements and a second-order accurate backward differentiation formula (BDF2) for the time-stepping. The domain walls are $90d_p$ wide, and particle P_0 is centered relative to these walls (a configuration similar to that used in the ANN database creation; see Fig. 1). The domain depth varies by case, ensuring that it is sufficient

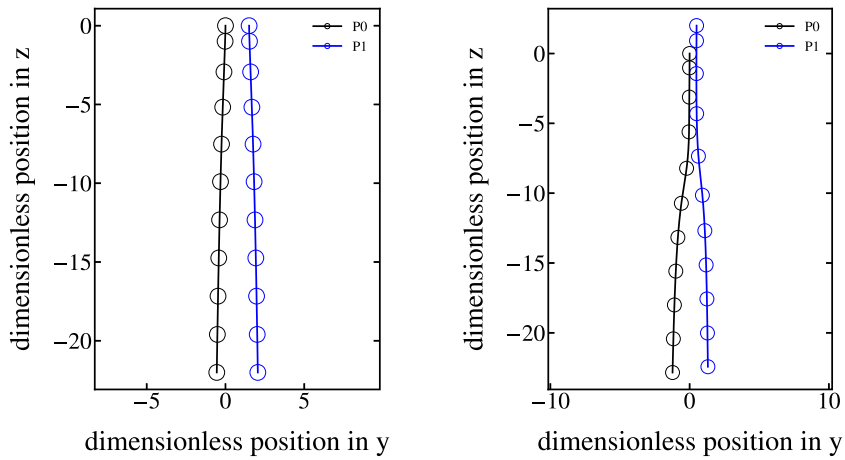

Fig. 8. Typical trajectory for both initial dispositions of the particles; (a) $r^* = 1.5$, $\theta = \frac{\pi}{2}$ and (b) $r^* = 2.06$, $\theta = 0.245$).

Table 6
The initial condition for the sedimentation of two particles is defined by a set of 4 dimensionless numbers assuming that the particles are initially at rest and identical. The vector $\boldsymbol{r_{01}}$ is the relative position vector going from particle P_0 center to particle P_1 center.

Variables	Number of components	Dimensions	Associated dimensionless numbers
d_p	1	L	repeating variable
ρ_f	1	ML^{-3}	repeating variable
ρ_p	1	ML^{-3}	$\rho^* = \frac{\rho_p}{\rho_f}$
μ	1	$ML^{-1}T^{-1}$	repeating variable
$\boldsymbol{r_{01}}$	2	L	$r^* = \frac{\lVert \boldsymbol{r} \rVert}{d_p}$, $\theta = acos\left(\frac{-\boldsymbol{g}\cdot\boldsymbol{r}}{\lVert \boldsymbol{g} \rVert \lVert \boldsymbol{r} \rVert}\right)$
$\lVert g \rVert$	1	$m\,s^{-2}$	$\mathrm{Ar} = \frac{\lVert \boldsymbol{g} \rVert d_p^3 \rho_f (\rho_p - \rho_f)}{\mu^2}$

Table 7
The 12 sedimentation cases used to characterize the predictive capability of the ROM.

Case	r^*	θ	Ar	ρ^*
1	1.5	$\frac{\pi}{2}$	20	1.5
2	1.5	$\frac{\pi}{2}$	319	1.5
3	1.5	$\frac{\pi}{2}$	2930	1.5
4	1.5	$\frac{\pi}{2}$	20	1000
5	1.5	$\frac{\pi}{2}$	319	1000
6	1.5	$\frac{\pi}{2}$	2930	1000
7	2.06	0.245	20	1.5
8	2.06	0.245	319	1.5
9	2.06	0.245	2930	1.5
10	2.06	0.245	20	1000
11	2.06	0.245	319	1000
12	2.06	0.245	2930	1000

to observe particle–particle interactions before they reach the bottom of the container. A refinement zone, shaped like a shell with an outer diameter of $1.4d_p$ and an inner diameter of $0.7d_p$, surrounds each particle and is kept to the minimum mesh size used in the ANN database creation ($\Delta x = \frac{15}{512} d_p$) to ensure mesh-independent results. The rest of the domain is refined using the Kelly error estimator. Time steps (Δt) are selected to ensure that the particle velocity varies by less than 1% compared to time-step independent results.

The analysis is conducted using dimensionless variables. The dimensionless variables include time (t'), velocity components (v'_x, v'_y, v'_z), and angular velocity components (ω'_x, ω'_y, ω'_z). The reference dimensions are l_r for length, t_r for time, and m_r for mass. These reference dimensions are defined as follows:

$$l_r = d_p \tag{4}$$

$$t_r = \sqrt{\frac{d_p}{\lVert \boldsymbol{g} \rVert}} \tag{5}$$

$$m_r = \frac{d_p^3}{6}\pi\rho_p \tag{6}$$

4.1. ROM and resolved CFD-DEM comparison

The ROM results for each of the 12 sedimentation cases are analyzed by comparing the velocity components of both particles to the results of the resolved CFD-DEM simulations. The vertical, horizontal, and angular velocities are compared in Figs. 9, 10, and 11 respectively.

The vertical velocity results (in the z-direction) from the ROM simulations mostly agree with those from the resolved CFD-DEM simulation. The agreement is almost perfect for all cases with $\rho^* = 1000$. However, for all cases with $\rho^* = 1.5$, the acceleration of the particles is higher in the ROM. This is more significant for lower Archimedes numbers (Cases 1 and 7). In Cases 7 to 9, the discrepancy in the acceleration of the trailing particle (P_1) is more significant than what is observed for particle P_0 (e.g., Case 9).

The horizontal velocity results (in the y-direction) from the ROM show a significant discrepancy with the resolved CFD-DEM simulation in cases with $\rho^* = 1.5$. However, the results for cases with $\rho^* = 1000$ are generally good. In Cases 1 to 3, horizontal acceleration occurs as soon as the particles are released, unlike the resolved CFD-DEM results. As the particles get further apart, the ROM results align more closely with the resolved CFD-DEM. In Case 1, a noticeable shift in horizontal acceleration is observed when the particles reach the threshold for the lubrication force. In Cases 3 and 9, the horizontal attraction seen in the initial acceleration phase of the resolved CFD-DEM simulation is absent in the ROM. Case 9 shows the most discrepancy, where the

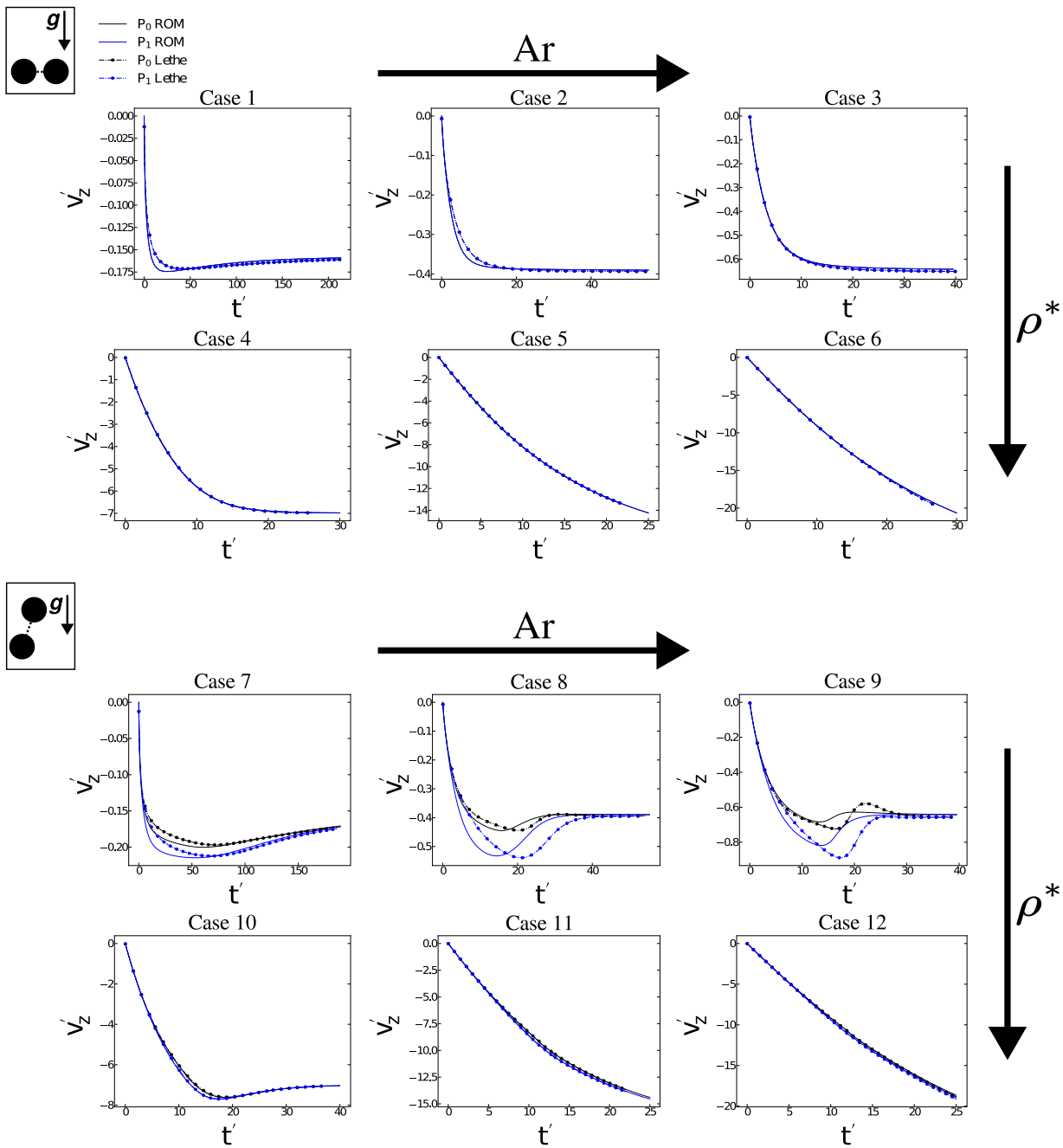

Fig. 9. Comparison of the vertical velocity results obtained with the ROM and the resolved CFD-DEM simulation. The Archimedes number (Ar) increases for each column to the right. For each of the two initial particles' dispositions, the ratio of the density ρ^* on the first line is 1.5 and 1000 on the second line.

kissing phase of the DKT interaction happens sooner, and the resulting horizontal velocity is much smaller. Minor discrepancies are observed for cases with $\rho^* = 1000$, with the largest relative discrepancy in Case 6. However, the ROM captures the dynamic interaction between the particles well. Notably, the DKT interactions in Cases 11 and 12, where the particles contact each other, match well with the resolved CFD-DEM simulations.

Similar to the horizontal velocity, the angular velocity results from the ROM for cases with $\rho^* = 1.5$ have a significant discrepancy with the resolved CFD-DEM. In the ROM, angular acceleration occurs earlier than in the resolved CFD-DEM simulations. For cases with $\rho^* = 1000$, Case 6 shows the largest discrepancy in angular velocity. In this case, the angular velocity of the ROM dissipates at a lower rate than in the resolved CFD-DEM simulation.

The norm of the relative velocity of the particles, relative to their sedimentation velocity in the DKT cases (Cases 7 to 12), is significantly higher when $\rho^* = 1.5$ (up to 20%) than when $\rho^* = 1000$ (up to 5%). The discrepancy in the horizontal velocity corresponds to a similar discrepancy in the angular velocity of the particles.

These observations indicate that the modification of the drag force induced by the other particle, the onset of the lift forces, and induced torque occur too soon in the ROM for cases with $\rho^* = 1.5$. According to the resolved CFD-DEM results, in cases with $\rho^* = 1.5$, the wake behind the particles establishes itself on a timescale similar to that required for the particle to reach its terminal velocity. However, in cases with $\rho^* = 1000$, the wake behind the particle establishes itself much faster than the time needed for the particles to reach their terminal velocity. Since the forces induced between the particles are modeled using a fully

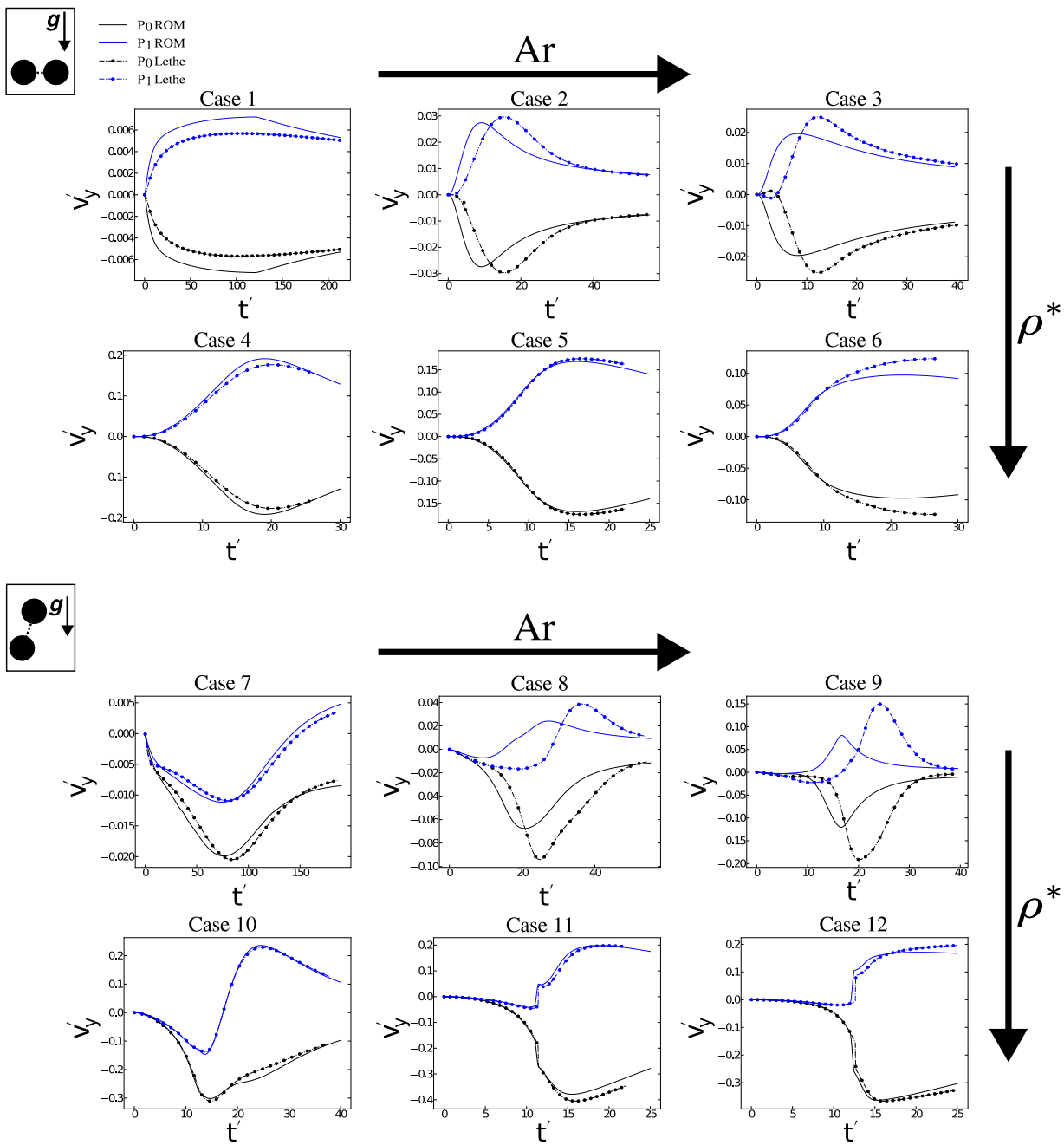

Fig. 10. Comparison of the horizontal velocity results obtained with the ROM and the resolved CFD-DEM simulation. The Archimedes number (Ar) increases for each column to the right. For each of the two initial particles' dispositions, the ratio of the density ρ^* on the first line is 1.5 and 1000 on the second line.

developed flow hypothesis, cases with $\rho^* = 1.5$ exhibit a significantly higher error in the acceleration phase, as the wake of the particle is not yet established. The fully developed flow hypothesis accurately models cases with $\rho^* = 1000$. This hypothesis for the force models is equivalent to considering an instantaneous fluid flow response time. As such, when the characteristic fluid response time t_f is smaller than the particle response time t_s, the fully developed flow hypothesis is more justified. A measure of the characteristic fluid response time is defined by dimensional analysis (see Appendix B), giving:

$$t_f = \frac{\rho_f d_p^2}{\mu} \tag{7}$$

A measure of the particle response time is given by the Stokes time (t_s)

$$t_s = \frac{(\rho_p + 0.5\rho_f)d_p^2}{18\mu} \tag{8}$$

The ratio of the two response times (t^*) is defined only by the density of the particles and the density of the fluid:

$$t^* = 18\frac{\rho_f}{\rho_p + 0.5\rho_f} \tag{9}$$

Small values of this ratio indicate that the fully developed flow assumption is valid for modeling the fluid force interaction between the

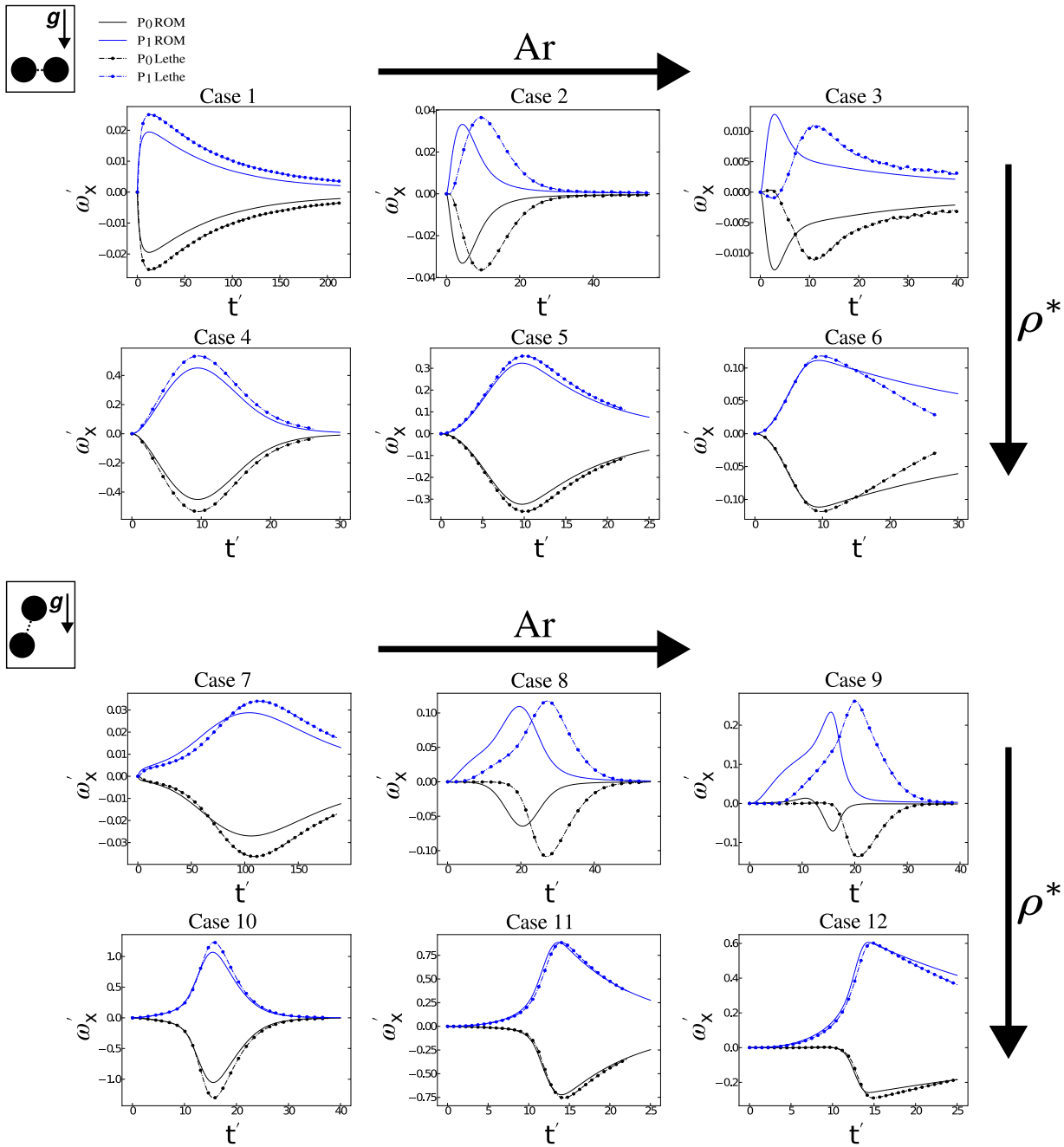

Fig. 11. Comparison of the angular velocity results obtained with the ROM and the resolved CFD-DEM simulation. The Archimedes number (Ar) increases for each column to the right. For each of the two initial particles' dispositions, the ratio of the density ρ^* on the first line is 1.5 and 1000 on the second line.

particles. Cases with $\rho^* = 1.5$ have a $t^* = 9$, and cases with $\rho^* = 1000$ have a $t^* = 0.018$, explaining why the particle interaction is adequately captured for cases with $\rho^* = 1000$.

This ratio underlines the effectiveness of using a fluid force model based on the assumption of fully developed flow for modeling particle interactions. In cases with $\rho^* = 1.5$, where $t^* = 9$, the slower response time impacts the accuracy of the model. Conversely, in cases with $\rho^* = 1000$, which have a $t^* = 0.018$, the rapid establishment of velocity profile ensures accurate modeling of the particle interactions with the fluid.

4.1.1. Effect of the density ratio

The results in Figs. 9, 10, and 11 underline a significant difference in the predictive capabilities of the ROM depending on the value of ρ^*. This is most notable in Cases 9 and 12, even though these two cases have the same Archimedes number and initial configuration of particles. To analyze the effect of ρ^*, its value is progressively increased from $\rho^* = 1.5$ to $\rho^* = 1000$ using the same configuration of particles and Archimedes number ($r^* = 2.06155$, $\theta = 0.24498$, and Ar $= 2930.541$). Discrepancies between the ROM and resolved CFD-DEM for values of ρ^* equal to 2, 4, 10, and 100 are added to the results obtained for Cases 9 and 12. Fig. 12 compares vertical and horizontal velocity results. The angular velocity and horizontal velocity discrepancy for these cases are similar; for this reason, it is not presented. These results demonstrate that as ρ^* increases, the ROM predictions align more closely with the results of the resolved CFD-DEM simulation. Results for cases with a $\rho^* = 100$ or higher are very well captured by the ROM, while results with $\rho^* = 10$ or smaller exhibit significant discrepancies. Also, the time

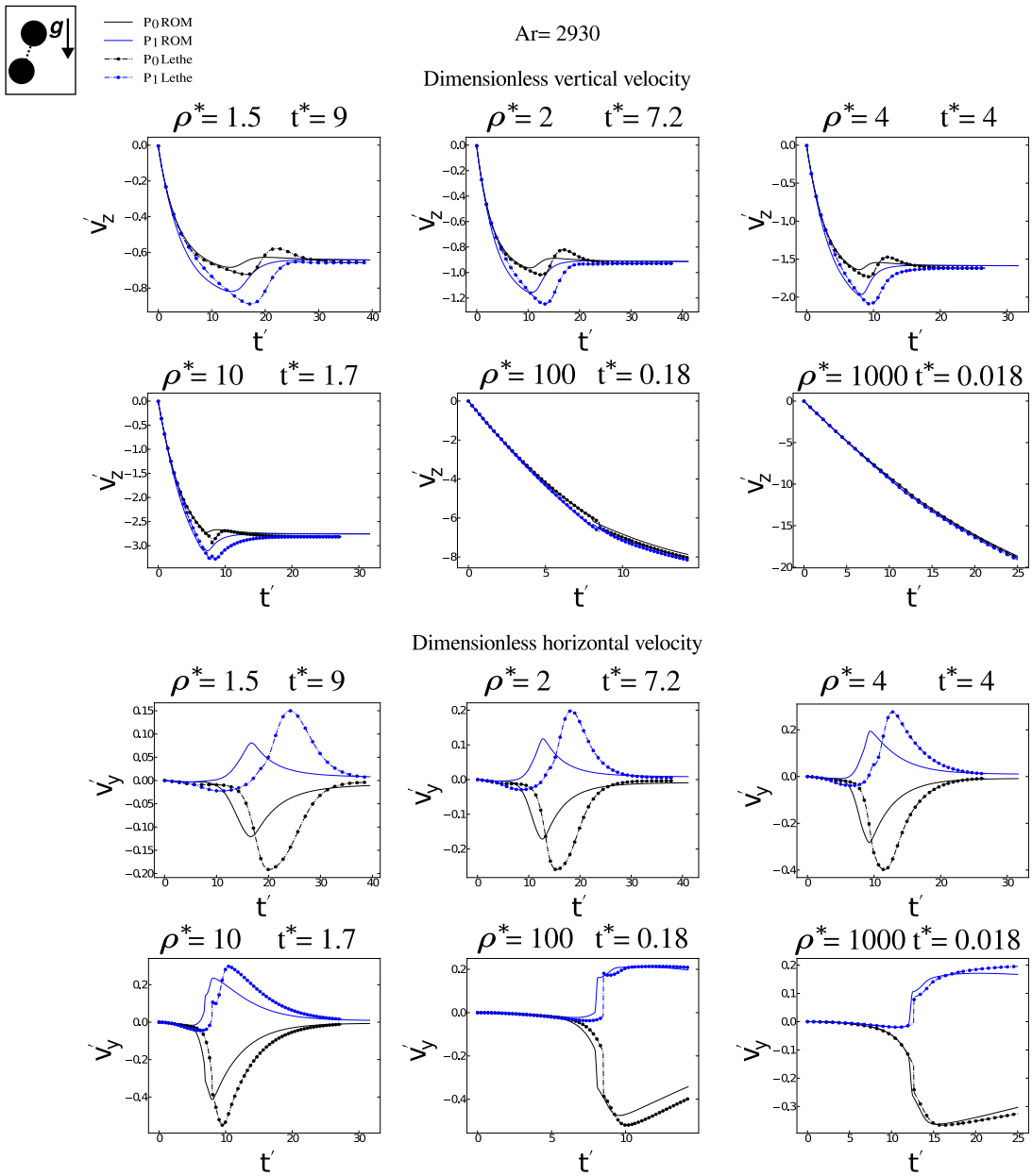

Fig. 12. Comparison of ROM vertical and horizontal particle velocity results with resolved CFD-DEM simulations for various ρ^*. For these cases $r^* = 2.06$, $\theta = 0.245$ and Archimedes number $Ar = 2930$.

misalignment between the results reduces progressively as ρ^* increases. These findings support the notion that premature particle interactions contribute to differences in the transient regime of the flow due to the fully developed flow hypothesis.

4.2. Effect of angular velocity

The dynamics of the particles presented in Section 4.1 suggest a link between the discrepancies in horizontal and angular velocities. The effect of angular velocity on the horizontal velocity of the particles is assessed by comparing the horizontal velocity in resolved CFD-DEM simulations when the particle rotation is locked versus when it is free (see Fig. 13). These results enable us to determine if the rotation of the particles could cause the differences observed in horizontal velocity. In these cases, the rotation of the particles increases dispersion. The horizontal velocities of Cases 9 and 12 are the most affected by the rotation of the particles, with a horizontal velocity up to 50% larger for particle P_1 when rotation is enabled. These results are consistent with the effect of the Magnus force on the particles. The horizontal velocities in cases with $\rho^* = 1.5$ with and without rotation converge to similar values as the particles' distance themselves. This is not observed in cases with $\rho^* = 1000$, indicating that horizontal particle displacement will be more affected by the absence of rotation in cases with higher ρ^*. These results also indicate that the impact of rotation on horizontal velocity is not significantly influenced by ρ^*. The effect of rotation is more pronounced in cases with larger Archimedes numbers (Cases 9 and 12), suggesting that the substantial differences observed in cases with lower density ratios are not linked to effects associated with particle rotation, supporting our hypothesis that it relates to the history of the flow.

4.3. Effects of the particles' relative velocity

As mentioned in Section 3, the relative velocity between the particles may also impact the drag, lift, and torque applied to the particles in

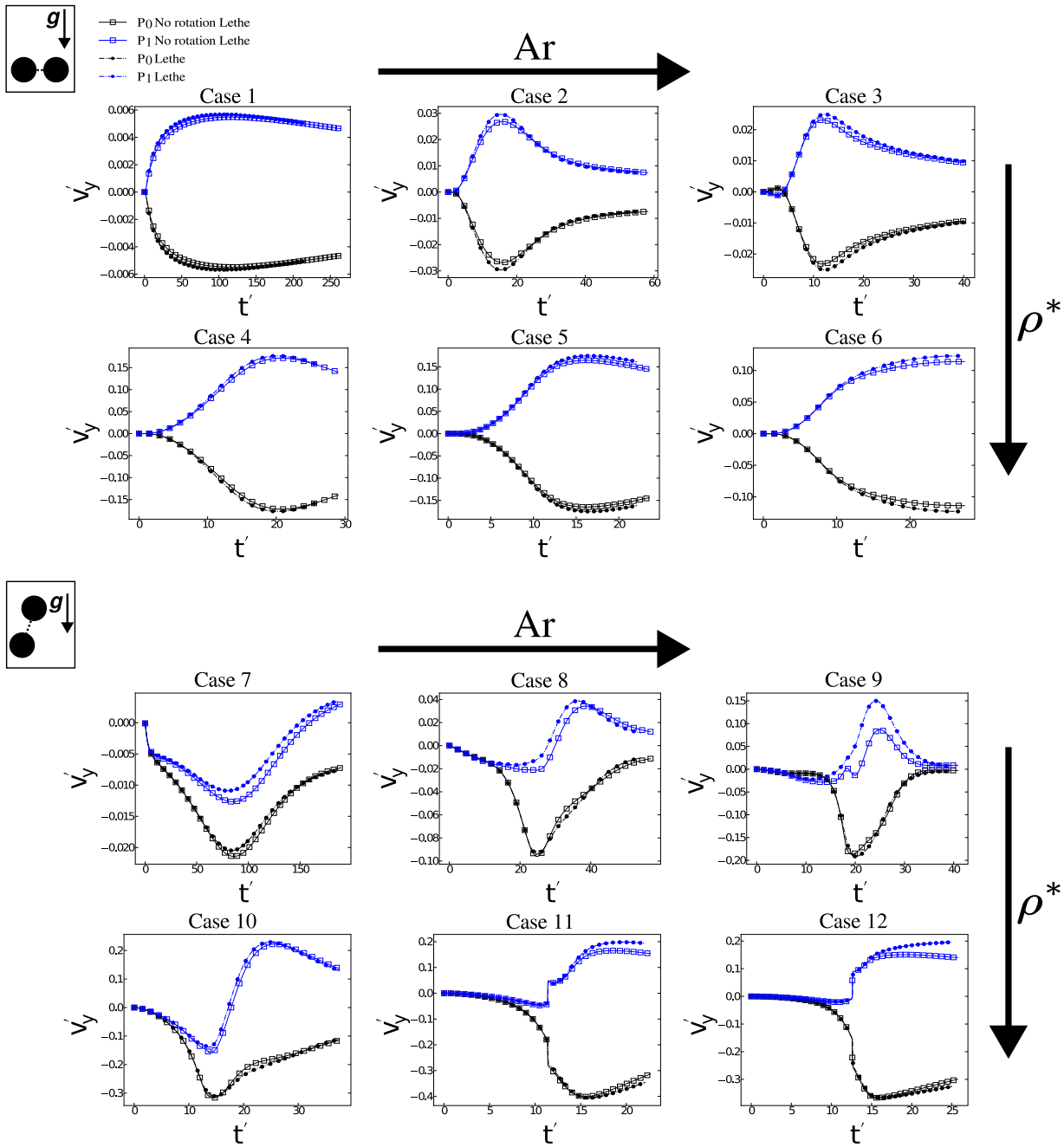

Fig. 13. Comparison of the horizontal velocity of resolved CFD-DEM simulation with and without the rotation of the particles. The rotation of the particle leads to a significant disparity in the horizontal velocity between the two simulations. The Archimedes number (Ar) increases for each column to the right. For each of the two initial particles' positions, the ratio of the density ρ^* on the first line is 1.5 and 1000 on the second line.

ways that the current ROM does not capture. A new dataset is generated to investigate whether the particles' relative velocity could explain the discrepancies observed between the ROM model and the resolved simulations. This dataset compiles the hydrodynamic force interaction between two particles, considering their relative velocity. The same strategy presented in Section 2 is used to generate the dataset. Additionally, the velocity of particle P1 is fixed at 0, and the second particle, moving around particle P1, is given a non-zero velocity. The change in the particle configuration due to the relative velocity between the particles would require a transient simulation, which would include transient effects on the force of the particle. However, to avoid these effects, the quasi-static hypothesis is used to isolate the impact of the difference in particle velocity. Consequently, a steady-state solution is used even though the relative velocity between the particles is non-zero. To limit the size of the sampling space, it is assumed that P2's velocity remains in the plane formed by P1's velocity ($\boldsymbol{v_1}$) and the center-to-center vector (r). The resulting particle configuration used for the simulation is presented in Fig. 14.

Using this setup, the drag, lift, and torque coefficients are evaluated solely on particle P1, as the wake direction of the particle in this simulation setup is determined by its velocity. The simulations are conducted in the reference frame of particle P1, which provides the basis for the dimensional analysis presented in Table 8. This variable space is sampled 2000 times using a Latin hypercube sampling method (McKay et al., 2000) within the bound defined in Table 9.

A parity plot is generated to assess if the current force models can capture the interaction of the particles due to their relative velocity,

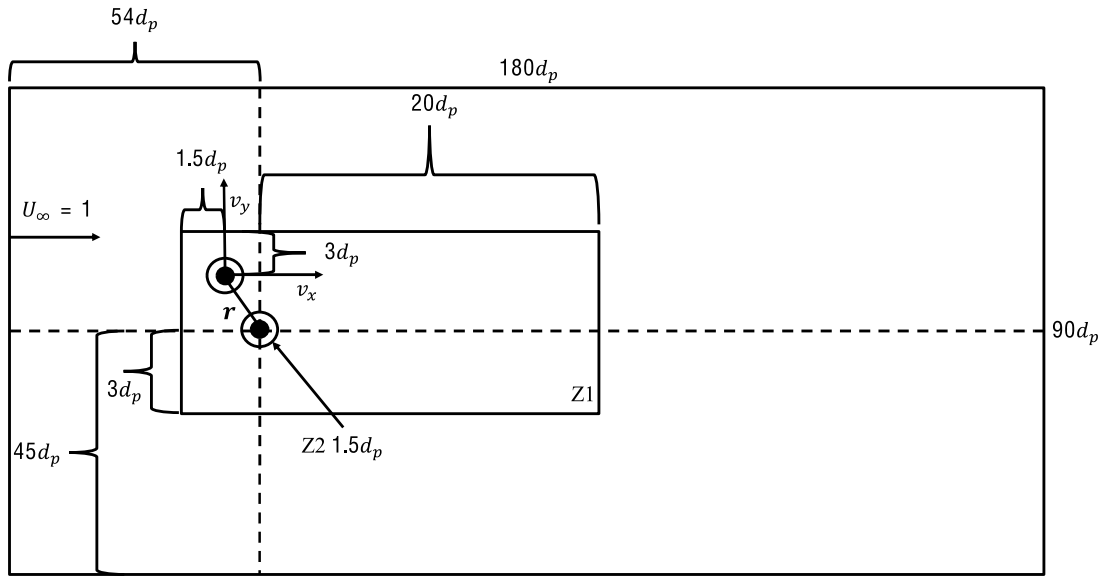

Fig. 14. Representation of the particles' disposition and the variable used to generate the dataset with the particle relative velocity, assuming a quasi-static particles' configuration. The same refinement zones around the particles (Z1 and Z2) are used.

Table 8
Dimensional analysis used to create a hydrodynamic force model that also considers the relative particle velocity.

Variables	Number of components	Dimensions	Associated dimensionless numbers
$\boldsymbol{f}$	2	MLT^{-2}	$Cd = \frac{-8F_{\parallel v}}{\rho_f d_p^2 \pi \lVert \boldsymbol{v} \rVert^2}$, $Cl = \frac{8F_{\perp v}}{\rho_f d_p^2 \pi \lVert \boldsymbol{v} \rVert^2}$
$\boldsymbol{T}$	1	$\mathrm{ML^2T^{-2}}$	$Ct = \frac{16 \lVert \boldsymbol{T} \rVert}{\rho_f d_p^3 \pi \lVert \boldsymbol{v} \rVert^2}$
d_p	1	L	repeating variable
ρ_f	1	$\mathrm{ML^{-3}}$	repeating variable
μ	1	$\mathrm{ML^{-1}T^{-1}}$	$Re = \frac{\lVert \boldsymbol{v} \rVert d_p \rho_f}{\mu}$
$\boldsymbol{r}$	2	L	$r^* = \frac{\lVert \boldsymbol{r} \rVert}{d_p}$, $\theta = acos\left(\frac{-\boldsymbol{v} \cdot \boldsymbol{r}}{\lVert \boldsymbol{v} \rVert \lVert \boldsymbol{r} \rVert}\right)$
$\boldsymbol{v} = \boldsymbol{v_1}$	1	$\mathrm{LT^{-1}}$	repeating variable
$\boldsymbol{v_2}$	2	$\mathrm{LT^{-1}}$	$v_x^* = \frac{v_\parallel}{\lVert \boldsymbol{v} \rVert}$, $v_y^* = \frac{v_\perp}{\lVert \boldsymbol{v} \rVert}$

Table 9
Sampling interval for each of the variables.

Variables	Sampled value
r^*	$\in [1.0625, 8]$
Re	$\in [0.1, 100]$
θ	$\in [0, \pi]$
v_x^*	$\in [-0.35, 0.35]$
v_y^*	$\in [-0.35, 0.35]$

as discussed in Section 3. This analysis is presented in Fig. 15. These results indicate that the relative velocity of the particles significantly impacts the hydrodynamic force applied to them. The ANN drag model, presented in Section 2.1, shows a correlation of $R^2 = 0.604$, significantly lower than the $R^2 = 1.000$ it achieved on cases where there was no relative velocity between the particles. However, when the lubrication force model is included, the correlation improves to $R^2 = 0.781$. This comparison underscores the effect of the particles' relative velocity on the hydrodynamic force in a manner not captured by the lubrication force model alone. These effects can be modeled and incorporated into the ROM through the addition of new force models. This can then be used to assess the impact of this additional force on the accuracy of the ROM, using the same type of ANN as described in Section 2.

For this purpose, the ROM is supplemented with a set of three new force models ($\boldsymbol{f}_{ij}^{d_r}, \boldsymbol{f}_{ij}^{l_r}, \boldsymbol{T}_{ij}^{I_r}$). These models capture the differences between the simulation results of the dataset with relative velocity and the combination of the ANN force model from Section 2, including the lubrication force model. Details on the ANN procedure used to develop these force models are provided in Appendix A. Adding these terms to the ROM results in the following equations that consider the particle's relative velocity:

$$\frac{d\boldsymbol{v}_i}{dt} = \frac{1}{m_i}\left(\sum_{\substack{j=0\\ i\neq j}}^{1}\left(\boldsymbol{f}_{ij}^{c} + \boldsymbol{f}_{ij}^{lub} + \boldsymbol{f}_{ij}^{d} + \boldsymbol{f}_{ij}^{l} + \boldsymbol{f}_{ij}^{v} + \boldsymbol{f}_{ij}^{m} + \boldsymbol{f}_{ij}^{d_r} + \boldsymbol{f}_{ij}^{l_r}\right) + \boldsymbol{f}_i^{h} + \boldsymbol{f}_i^{mag} + \boldsymbol{f}_i^{b}\right) \tag{10}$$

$$\frac{d\boldsymbol{\omega}_i}{dt} = \frac{1}{I_i}\left(\sum_{\substack{j=0\\ i\neq j}}^{1}\left(\boldsymbol{T}_{ij}^{I} + \boldsymbol{T}_{ij}^{lub} + \boldsymbol{T}_{ij}^{I_r}\right) + \boldsymbol{T}_i^{v}\right) \tag{11}$$

The effect of these new force models on particle dynamics can be assessed using the modified ROM. Case 9, which shows the highest relative velocity between particles, is used for this purpose. The results of the velocity comparison are shown in Figs. 16, 17, and 18, displaying the vertical, horizontal, and angular velocities, respectively. These results reveal that the discrepancy becomes more pronounced when the modified ROM is used. The premature interaction of the particles is still observable, indicating that the relative velocity is not the primary cause of the previously discussed discrepancies. The increased discrepancy between the model and the particle-resolved simulations demonstrates that the quasi-static particle configuration hypothesis used to generate this force model is inadequate and fails to improve the ROM's prediction quality. These observations suggest that the interaction of two moving particles is highly dependent on the

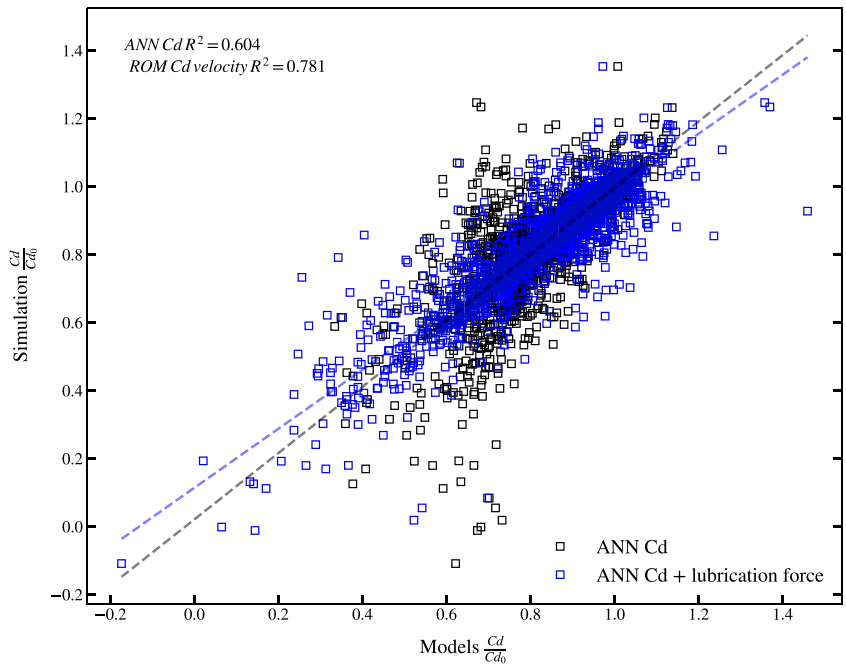

Fig. 15. Parity plot of the ANN model presented in Section 2 alone and combined with the lubrication force relative to the dataset with relative particle velocity.

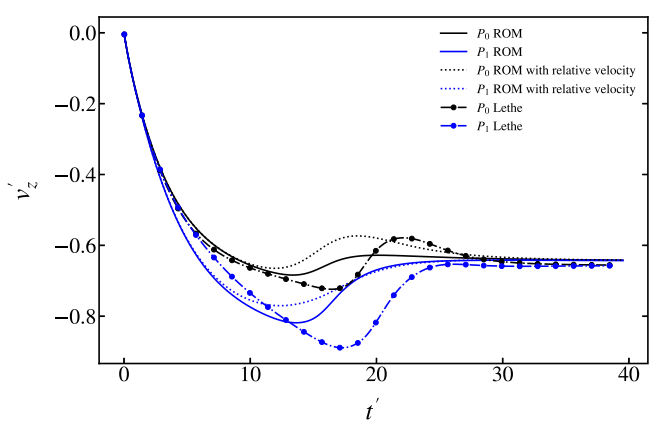

Fig. 16. Comparison of the vertical velocity obtained from the ROM, the ROM with the relative velocity effect, and particle resolved simulation using Lethe.

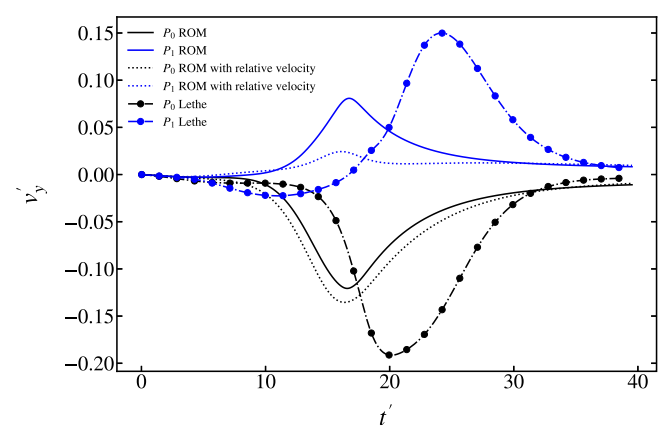

Fig. 17. Comparison of the horizontal velocity obtained from the ROM, the ROM with the relative velocity effect, and particle resolved simulation using Lethe.

history of their interaction with the fluid and their relative position, which are not captured by models built from simulations using the fully developed flow hypothesis.

5. Conclusion

This study represents a comprehensive demonstration that the history of particle interactions plays a critical role in particle dynamic interaction, offering new insights into fluid–solid modeling. To conduct this study, an ANN fluid–solid force model for the fluid force interaction of a pair of particles (induced drag, lift, and torque) was developed, as detailed in Section 2. This force model was constructed under the fully developed flow hypothesis without considering the particles' rotation. This is a common approach in the creation of general fluid force models for large-scale fluid–solid modeling, such as unresolved CFD-DEM simulations. Two versions of the model are discussed and analyzed: one that does not take into account the effect of the particles' relative velocity (see Section 2) and one that does consider the particles' relative velocity (see Section 4.3). These force models show root mean square errors of less than 2% and 4%, respectively, with an untrained test dataset. Using this fluid–solid force model, Section 4.1 introduces a Reduced Order Model (ROM) for the sedimentation of a pair of particles. Section 4 then uses the ROM to analyze the dynamics obtained and compares them to resolved CFD-DEM simulations. The conclusions drawn from this analysis process are as follows:

- For cases where the fluid response time is in the same order of magnitude as the particle response time or larger, the development of the wake plays an important role in the induced fluid forces and torque. In these cases, the fully developed flow hypotheses lead to premature interaction between the particles. This indicates that the particles' interaction history plays an important role in their dynamics.
- Modeling the effect of particles' relative velocity using a quasi-static hypothesis deteriorates the ROM's predictive capability. This implies that relative particle motion should be modeled dynamically to capture the particles' interaction accurately. This also indicates that the error observed in the ROM does not stem from neglecting the particle relative velocity in the hydrodynamic force model.

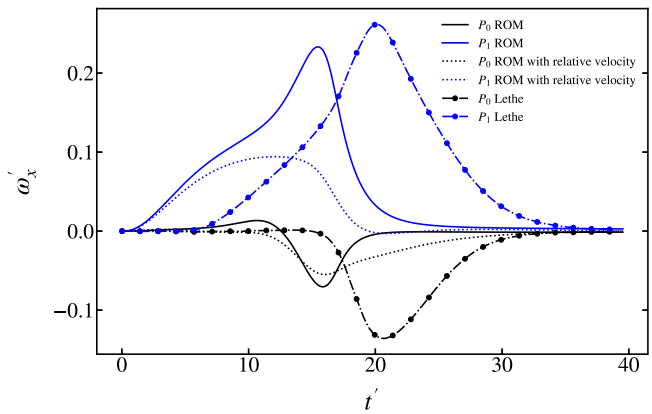

Fig. 18. Comparison of the angular velocity obtained from the ROM, the ROM with the relative velocity effect, and particle resolved simulation using Lethe.

- The induced drag and lift force and induced torque model based on the fully developed hypothesis is adequate to model these forces when the fluid response time (t_f) is much smaller than the particle response time (t_s). This means t^* should be smaller than 1.
- The rotation of particles plays a role in particle dispersion. However, it is not more significant for lower values of ρ^*. The impact of rotation was higher for cases with higher Archimedes numbers (higher Reynolds numbers).

These conclusions suggest that further development of solid–fluid force models, incorporating the relative position of particles as explored by Akiki et al. (2017), Cheng and Wachs (2023), van Wachem et al. (2024) and Seyed-Ahmadi and Wachs (2020), could substantially decrease modeling errors in gas–solid applications. This study also hypothesizes that errors from the fully developed flow hypothesis might also affect other drag models that rely on similar assumptions, potentially leading to premature drag reduction during particle acceleration in liquid–solid systems. This implies that liquid–solid interactions modeled with these types of fluid–solid force models will include errors due to premature particle interaction, similar to what was observed in cases with $\rho^* = 1.5$. Due to the anisotropy of particles' interaction and history effects, the mean of this error is most likely not zero in cases with large numbers of particles. This means it would result in a measurable effect on the dynamics of particle clusters.

Furthermore, the research indicates that neglecting transient hydrodynamic forces, such as virtual mass and history forces, can lead to inaccuracies similar to those caused by premature particle interactions, as demonstrated by Nijssen et al. (2020) and Ferreira et al. (2023). Their findings highlight the challenges in finding drag correlations that accurately replicate the dynamics in liquid fluidized beds, especially with particles having a ρ^* close to one.

The impact of the fully developed flow hypothesis on the drag and induced lift force model has been well established in this study. This highlights the challenges in accurately modeling liquid–solid mixing and opens exciting avenues to enhance our understanding and modeling of solid–liquid interactions, particularly where complex history effects influence particle interactions. Studying this phenomenon in larger systems would be a valuable contribution to the understanding of solid–fluid interactions. This newfound awareness paves the way for more precise and insightful models, fostering a promising future in applications that involve solid–liquid flows.

CRediT authorship contribution statement

Lucka Barbeau: Writing – original draft, Visualization, Validation, Software, Methodology, Investigation, Formal analysis, Data curation, Conceptualization. **Stéphane Étienne:** Writing – review & editing, Formal analysis. **Cédric Béguin:** Writing – review & editing, Validation. **Bruno Blais:** Writing – review & editing, Supervision, Resources, Methodology, Investigation, Funding acquisition, Formal analysis.

Declaration of competing interest

The authors declare the following financial interests/personal relationships which may be considered as potential competing interests: Bruno Blais reports financial support was provided by Natural Sciences and Engineering Research Council of Canada. Lucka Barbeau reports financial support was provided by Natural Sciences and Engineering Research Council of Canada. Bruno Blais reports equipment, drugs, or supplies was provided by Digital Research Alliance of Canada.

Data availability

The code is available on a GitHub repository reference in the article.

Acknowledgments

The authors would like to acknowledge the financial support from the Natural Sciences and Engineering Research Council of Canada (NSERC) through the RGPIN-2020-04510 Discovery grant. In particular, Lucka Barbeau would like to acknowledge an NSERC CREATE Simulation-Based Engineering Science (SBES) scholarship. The authors would also like to acknowledge the technical support and computing time provided by the Digital Research Alliance of Canada.

Appendix A. Force models details

This appendix presents each of the force models used in the ROM. Note that the drag force, lift force, and induce torque models are presented in Section 2.

A.1. Drag force

The drag force applied to the particle is defined by the ANN regression. The regression is performed on data scaled by the drag coefficient of a single particle (see Eq. (1)), implying that it must be multiplied back by the drag coefficient of a single particle (Cd_0).

$$Cd = Cd_0(\mathrm{Re})Cd_{ANN}(\mathrm{Re}, r^*, \theta) \tag{A.1}$$

$$\boldsymbol{f}_i^d = -\frac{1}{8}\rho_f \pi d_p^2 Cd \boldsymbol{v}_i \parallel \boldsymbol{v}_i \parallel \tag{A.2}$$

The resulting expression for drag correlation is too complex to detail here. For example, the resulting coefficient mapping as a function of the particle position relative to a reference particle for a given Reynold number of 10 is presented in Fig. A.19. Cd_{ANN}

A.2. Lift force

The lift force applied to the particle is defined by the ANN regression. The regression is performed on data scaled by the drag coefficient of a single particle (see Eq. (1)), implying that it must be multiplied back by the drag coefficient of a single particle (Cd_0).

$$Cl = Cd_0(\mathrm{Re})Cl_{ANN}(\mathrm{Re}, r^*, \theta) \tag{A.3}$$

$$\boldsymbol{r}_\perp = \boldsymbol{r} - \frac{\boldsymbol{r}\cdot\boldsymbol{v}_i}{\parallel \boldsymbol{v}_i \parallel^2}\boldsymbol{v}_i \tag{A.4}$$

$$\boldsymbol{f}_i^l = \frac{1}{8}\rho_f \pi d_p^2 Cl \parallel \boldsymbol{v}_i \parallel^2 \frac{\boldsymbol{r}_\perp}{\parallel \boldsymbol{r}_\perp \parallel} \tag{A.5}$$

The resulting expression for lift correlation is too complex to detail here. For example, the resulting coefficient mapping as a function of the particle position relative to a reference particle for a given Reynold number of 10 is presented in Fig. A.20.

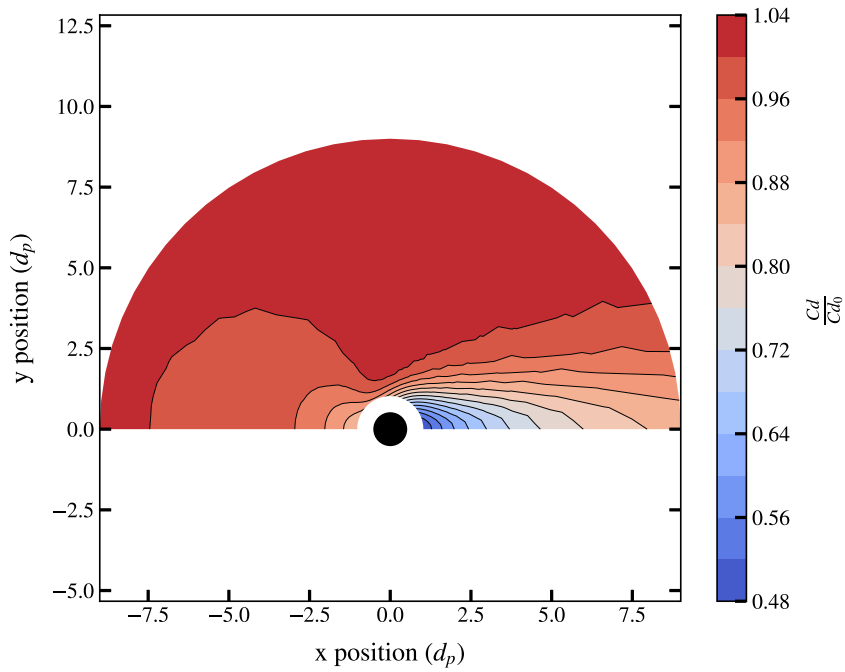

Fig. A.19. Drag coefficient correction factor at a Reynold number of 10. In this figure, the velocity of the particle is negative in x.

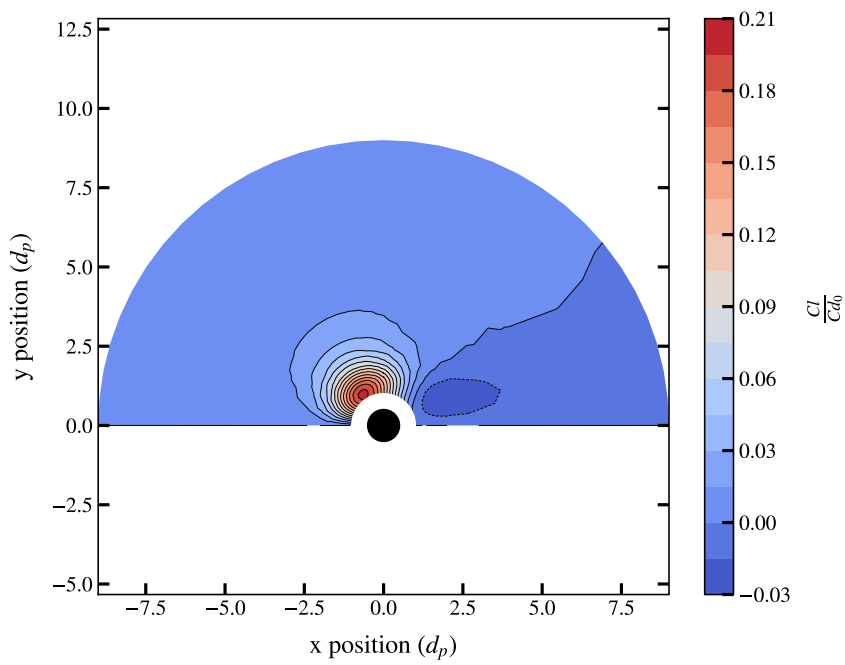

Fig. A.20. Lift coefficient correction factor at a Reynold number of 10. In this figure, the velocity of the particle is negative in x.

A.3. History force

The history force model use is defined based on the work of Parmar et al. (2018) and Dorgan and Loth (2007), both works are based on the work of Mei and Adrian (1992). The history force is decomposed into two components: the near proper history $\boldsymbol{f}^h_{i,near}$ and the improper history $\boldsymbol{f}^h_{i,imp}$ that contains the singularity of the history kernel. Here, we drop the far-history terms and only conserve the near-history terms since the evaluation cost of the full history in the case of two particles is not prohibitive.

$$\boldsymbol{f}^h_i = \boldsymbol{f}^h_{i,imp} + \boldsymbol{f}^h_{i,near} \tag{A.6}$$

The two terms are defined as follows. The subscript $_r$ refers to the particle state at the initial time step. Since the particles are at rest at the initial time step, a Reynolds number of $1e-3 Re_{v_f}$ is used to evaluate the initial particle state. Here, v_f is the terminal velocity of the particle.

$$c_1 = 2.5 \tag{A.7}$$

$$c_2 = 0.126 \tag{A.8}$$

$$gH = \frac{0.75 + c_2 Re}{Re} \tag{A.9}$$

$$t_r = \frac{d_p^2 \rho}{4\mu} \left(\frac{256}{\pi}\right)^{\frac{1}{3}} gH_r^2 \tag{A.10}$$

$$m_r = \frac{3}{4}\sqrt{\pi} d_p^3 \rho_f \left(\frac{256}{\pi}\right)^{\frac{1}{6}} g H_r \tag{A.11}$$

$$l_r = \frac{d_p}{2} \tag{A.12}$$

$$r_i = \left(\frac{g H_r}{g H}\right)^{\frac{3}{2}} \tag{A.13}$$

$$\Delta t^* = \Delta t / t_r \tag{A.14}$$

$$\gamma = r_i^{\frac{1}{3}} \Delta t^{*\frac{1}{4}} \tag{A.15}$$

$$K_0 = \frac{2}{9} r_i^{\frac{-2}{3}} (-0.3722\gamma + 12.16\gamma^2 - 6.488\gamma^3) \tag{A.16}$$

$$\boldsymbol{u}^* = \boldsymbol{u}\frac{t_r}{l_r} \tag{A.17}$$

$$\boldsymbol{v}_i^* = \boldsymbol{v}_i \frac{t_r}{l_r} \tag{A.18}$$

$$\boldsymbol{a} = \frac{d\boldsymbol{u}^*}{d\tau^*} - \frac{d\boldsymbol{v}_i^*}{d\tau^*} \tag{A.19}$$

$$\boldsymbol{f}_{i,imp}^h = K_0 \boldsymbol{a}|_{t^*} \frac{m_r l_r}{t_r^2} \tag{A.20}$$

$$K_i(t^*, \tau^*) = \left((t^* - \tau^*)^{\frac{1}{2c_1}} + r_i (t^* - \tau^*)\right)^{-c_1} \tag{A.21}$$

$$\boldsymbol{f}_{i,near}^h = \frac{m_r l_r}{t_r^2} \int_0^{t^* - \Delta t^*} K_i(t^*, \tau^*) \boldsymbol{a}|_{\tau^*} d\tau^* \tag{A.22}$$

The integral that defines $\boldsymbol{f}_{i,near}^h$ is evaluated using the trapezoidal rule over the history of the particle acceleration. The constant c_1 and c_2 are taken from Kim et al. (1998) works and seem to agree more with the simulation results than other values found in the literature.

A.4. Virtual mass and Meshchersky forces

The virtual mass force for a pair of particles is derived from the work of Béguin et al. (2016). In a pair of particles with index 0 and 1, the virtual mass force on the particle 0 ($\boldsymbol{f}_0^v$) is defined as follows.

$$C_{m,\perp,\perp} = \frac{1}{2}\left[1 + \frac{3}{256}\left(\frac{d_p}{\| \boldsymbol{r} \|}\right)^6 + \frac{3}{256}\left(\frac{d_p}{\| \boldsymbol{r} \|}\right)^8 + \frac{27}{4096}\left(\frac{d_p}{\| \boldsymbol{r} \|}\right)^{10}\right] \tag{A.23}$$

$$C_{m,\|,\|} = \frac{1}{2}\left[1 + \frac{3}{64}\left(\frac{d_p}{\| \boldsymbol{r} \|}\right)^6 + \frac{9}{256}\left(\frac{d_p}{\| \boldsymbol{r} \|}\right)^8 + \frac{9}{512}\left(\frac{d_p}{\| \boldsymbol{r} \|}\right)^{10}\right] \tag{A.24}$$

$$C_{m,\perp,\perp}^i = \frac{1}{2}\left[\frac{3}{16}\left(\frac{d_p}{\| \boldsymbol{r} \|}\right)^3 + \frac{3}{4096}\left(\frac{d_p}{\| \boldsymbol{r} \|}\right)^9 + \frac{3}{2048}\left(\frac{d_p}{\| \boldsymbol{r} \|}\right)^{11}\right] \tag{A.25}$$

$$C_{m,\|,\|}^i = -\frac{1}{2}\left[\frac{3}{8}\left(\frac{d_p}{\| \boldsymbol{r} \|}\right)^3 + \frac{3}{512}\left(\frac{d_p}{\| \boldsymbol{r} \|}\right)^9 + \frac{9}{1024}\left(\frac{d_p}{\| \boldsymbol{r} \|}\right)^{11}\right] \tag{A.26}$$

$$\boldsymbol{R} = \begin{bmatrix} r_x^2 & r_x r_y & r_x r_z \\ r_y r_x & r_y^2 & r_y r_z \\ r_z r_x & r_z r_y & r_z^2 \end{bmatrix} \tag{A.27}$$

$$\boldsymbol{M} = -\rho_f \frac{\pi d_p^3}{6}\left[(C_{m,\|,\|} - C_{m,\perp,\perp})\boldsymbol{R} - C_{m,\perp,\perp}\boldsymbol{\delta_{ij}}\right] \tag{A.28}$$

$$\boldsymbol{M}^i = -\rho_f \frac{\pi d_p^3}{6}\left[(C_{m,\|,\|}^i - C_{m,\perp,\perp}^i)\boldsymbol{R} - C_{m,\perp,\perp}^i\boldsymbol{\delta_{ij}}\right] \tag{A.29}$$

$$\boldsymbol{f}_0^v = \boldsymbol{M}\frac{d\boldsymbol{v_0}}{dt} + \boldsymbol{M}^i \frac{d\boldsymbol{v_1}}{dt} \tag{A.30}$$

In these equations, the δ_{ij} is the Kronecker delta, and the variables r_x, r_y and r_z are the three spacial components of the vector $\boldsymbol{r}$. These coefficients are obtained by keeping only the first three terms of the infinite series that define these coefficients.

The Meshchersky force represents the force due to the virtual mass force coefficient variation. It is defined in the work of Zoghlami et al. (2019). Using the previously defined variables for the virtual mass force. The Meshchersky force is defined as follows:

$$\boldsymbol{f}_0^m = \frac{d\boldsymbol{M}}{dt}\boldsymbol{v_0} + \frac{d\boldsymbol{M}^i}{dt}\boldsymbol{v_1} \tag{A.31}$$

A.5. Lubrication force

The lubrication force model is defined using the model of Cooley et al. and O'Neil et al. (Cooley and O'neill, 1969; O'Neill and Majumdar, 1970). The implementation is based on the work of Simeonov et al. (Simeonov and Calantoni, 2012).

$$\epsilon = 2\frac{\| \boldsymbol{r} \| - \frac{d_{p_i} + d_{p_j}}{2}}{d_{p_i}} \tag{A.32}$$

$$\kappa = \frac{d_{p_i}}{d_{p_j}} \tag{A.33}$$

$$\epsilon_{max} = 4 \tag{A.34}$$

$$\boldsymbol{e_{ij}} = \frac{\boldsymbol{r_{ij}}}{\| \boldsymbol{r_{ij}} \|} \tag{A.35}$$

$$\boldsymbol{v_{ij}} = \boldsymbol{v_j} - \boldsymbol{v_i} \tag{A.36}$$

$$\boldsymbol{\omega_{ij}} = \boldsymbol{\omega_j} + \boldsymbol{\omega_i} \tag{A.37}$$

$$\boldsymbol{f_i^{lub^n}} = \left(\frac{\kappa^2}{(1+\kappa)^2}\left(\frac{1}{\epsilon} - \frac{1}{\epsilon_{max}}\right) - \frac{\kappa(1+7\kappa+\kappa^2)}{5(1+\kappa)^3} ln\left(\frac{\epsilon}{\epsilon_{max}}\right)\right) \cdot 3\pi\mu d_{p_i} \boldsymbol{v_{ij}} \cdot \boldsymbol{e_{ij}}\boldsymbol{e_{ij}} \tag{A.38}$$

$$\boldsymbol{f_i^{lub^{tt}}} = -\left(\frac{4\kappa(2+\kappa+2\kappa^2)}{15(1+\kappa)^3} ln\left(\frac{\epsilon}{\epsilon_{max}}\right)\right) \cdot 3\pi\mu d_{p_i}\left(\boldsymbol{v_{ij}} - \boldsymbol{v_{ij}} \cdot \boldsymbol{e_{ij}}\boldsymbol{e_{ij}}\right) \tag{A.39}$$

$$\boldsymbol{f_i^{lub^{tr}}} = 1.5\pi\mu d_{p_i}^2 \frac{2\kappa^2}{15(1+\kappa)^2} ln\left(\frac{\epsilon}{\epsilon_{max}}\right)(\boldsymbol{\omega_{ij}} + 4\kappa^{-1}\boldsymbol{\omega_i} + 4\kappa\boldsymbol{\omega_j})\boldsymbol{e_{ij}} \tag{A.40}$$

$$\boldsymbol{f_i^{lub^*}} = \boldsymbol{f_i^{lub^n}} + \boldsymbol{f_i^{lub^{tt}}} + \boldsymbol{f_i^{lub^{tr}}} \tag{A.41}$$

$$\boldsymbol{T_i^{lub^{tt}}} = -2\pi\mu d_{p_i}^2\left(\frac{\kappa(4+\kappa)}{10(1+\kappa)^2} ln\left(\frac{\epsilon}{\epsilon_{max}}\right)\right)\boldsymbol{e_{ij}} \times \boldsymbol{v_{ij}} \tag{A.42}$$

$$\boldsymbol{T_i^{lub^{tr}}} = \pi\mu d_{p_i}^3 \frac{2\kappa}{5(1+\kappa)^2} ln\left(\frac{\epsilon}{\epsilon_{max}}\right)\left(\left(\boldsymbol{\omega_i} + \frac{\kappa\boldsymbol{\omega_j}}{4}\right) - \left(\boldsymbol{\omega_i} + \frac{\kappa\boldsymbol{\omega_j}}{4}\right) \cdot \boldsymbol{e_{ij}}\boldsymbol{e_{ij}}\right) \tag{A.43}$$

$$\boldsymbol{T_i^{lub^*}} = \boldsymbol{T_i^{lub^{tt}}} + \boldsymbol{t_i^{lub^{tr}}} \tag{A.44}$$

To avoid the singularity when two particles are in contact in the current models, we also limit the dimensionless minimal interparticle distance (ϵ) to ϵ_{min}. This model is valid in the limit of creeping flow, meaning the gap between the particles must be sufficiently small to obtain accurate results. For this reason, we add a threshold to limit the application of this force model when the interparticle distance is above a given threshold (ϵ_{max}). Outside of this threshold, the lubrication force is 0. To avoid a jump in the force applied to the particle, we subtract the lubrication force associated with the maximal gap (ϵ_{max}), which gives the following model.

$$\boldsymbol{f_i^{lub}} = \begin{cases} 0 & \epsilon > \epsilon_{max} \\ \boldsymbol{f_i^{lub^*}} & \epsilon \leq \epsilon_{max} \ \& \ \epsilon > \epsilon_{min} \\ \boldsymbol{f_i^{lub^*}}|_{\epsilon=\epsilon_{min}} & \epsilon \leq \epsilon_{min} \end{cases} \tag{A.45}$$

$$\boldsymbol{T_i^{lub}} = \begin{cases} 0 & \epsilon > \epsilon_{max} \\ \boldsymbol{T_i^{lub^*}} & \epsilon \leq \epsilon_{max} \ \& \ \epsilon > \epsilon_{min} \\ \boldsymbol{T_i^{lub^*}}|_{\epsilon=\epsilon_{min}} & \epsilon \leq \epsilon_{min} \end{cases} \tag{A.46}$$

In this paper, $\epsilon_{max} = 4$ and $\epsilon_{min} = \frac{1}{32}$. ϵ_{min} can be interpreted as a measure of surface roughness. $\epsilon_{max} = 2d_p$ was obtained through calibration of the contact lubrication dynamics of the Ten Cate experiments.

A.6. Magnus force

The Magnus lift is obtained using the correlation proposed by Loth (2008).

$$\Omega^* = \frac{\| \boldsymbol{\omega_i} \| d_p}{\| \boldsymbol{u} - \boldsymbol{v_i} \|} \tag{A.47}$$

$$C_{l,\Omega} = 1 - \left[0.675 + 0.15\left(1 + tanh(0.28(\Omega^* - 2))\right)\right] \tag{A.48}$$

$$\boldsymbol{f_i^{mag}} = \frac{\pi}{8} d_p^3 \rho_f \left[C_{l,\Omega}(\boldsymbol{u} - \boldsymbol{v_i}) \times \boldsymbol{\omega_i}\right] \tag{A.49}$$

A.7. Contact force

The contact force is derived from the linear contact model of Cundall et al. (Cundall and Strack, 1979), and its implementation in Lethe (Golshan et al., 2023).

$$l = \| \boldsymbol{r} \| - \frac{d_{p_i} + d_{p_j}}{2} \tag{A.50}$$

$$\delta_n = \begin{cases} -l & l < 0 \\ 0 & \text{otherwise} \end{cases} \tag{A.51}$$

$$\boldsymbol{v_{ij}} = \frac{d\boldsymbol{r}}{dt} + (0.5 d_p \boldsymbol{\omega_0} + 0.5 d_p \boldsymbol{\omega_1}) \times \frac{\boldsymbol{r}}{\| \boldsymbol{r} \|} \tag{A.52}$$

$$\boldsymbol{v_{rt}} = \boldsymbol{v_{ij}} - \left(\boldsymbol{v_{ij}} \cdot \frac{\boldsymbol{r}}{\| \boldsymbol{r} \|}\right) \frac{\boldsymbol{r}}{\| \boldsymbol{r} \|} \tag{A.53}$$

$$\boldsymbol{\delta_t} = \int_{t_{c0}}^{t} \boldsymbol{v_{rt}} dt \tag{A.54}$$

$$r_e = \left(\frac{2}{d_{p_0}} + \frac{2}{d_{p_1}}\right)^{-1} \tag{A.55}$$

$$m_e = \left(\frac{1}{m_0} + \frac{1}{m_1}\right)^{-1} \tag{A.56}$$

$$Y_e = \left(\frac{1}{Y_0} + \frac{1}{Y_1}\right)^{-1} \tag{A.57}$$

$$k_n = \frac{16}{15}\sqrt{r_e} Y_e \left(\frac{15 m_e \| \boldsymbol{v_{ij}}|_{t_{c0}} \|^2}{16\sqrt{r_e} Y_e}\right)^{\frac{1}{5}} \tag{A.58}$$

$$c_n = \frac{-2ln(e)}{\sqrt{(ln(e))^2 + \pi^2}} \sqrt{m_e k_n} \tag{A.59}$$

$$k_t = 0.4 k_n \tag{A.60}$$

$$c_t = \frac{-2ln(e)}{\sqrt{(ln(e))^2 + \pi^2}} \sqrt{m_e k_t} \tag{A.61}$$

$$\boldsymbol{f^{c_n}} = -\left(k_n \delta_n + c_n \frac{d\delta_n}{dt}\right) \frac{\boldsymbol{r}}{\| \boldsymbol{r} \|} \tag{A.62}$$

$$\boldsymbol{f^{c_t^*}} = -k_t \boldsymbol{\delta_t} - c_t \frac{d\boldsymbol{\delta_t}}{dt} \tag{A.63}$$

$$\boldsymbol{f^{c_t}} = \begin{cases} \boldsymbol{f^{c_t^*}} & \| \boldsymbol{f^{c_t^*}} \| < \mu_c \| \boldsymbol{f^{c_n}} \| \\ \boldsymbol{f^{c_t^*}} \frac{\| \boldsymbol{f^{c_n}} \| \mu_c}{\| \boldsymbol{f^{c_t^*}} \|} & \text{otherwise} \end{cases} \tag{A.64}$$

$$\boldsymbol{f^c} = \boldsymbol{f^{c_n}} + \boldsymbol{f^{c_t}} \tag{A.65}$$

In these equations, m_i is the mass of the particle i, Y_i is the Young's modulus of the particle, e is the effective restitution coefficient, μ_c is the contact friction coefficient, t_{c0} is the initial point in time where the particle contact. With this force, we can define the contact torques as follows:

$$\boldsymbol{T^c} = \boldsymbol{f^{c_t}} \times \frac{\boldsymbol{r} d_p}{2 \| \boldsymbol{r} \|} \tag{A.66}$$

For all cases presented in the current work, the friction coefficient was set to 0, the restitution coefficient to 1, and the Young modulus to 10 MPa. The young modulus is small since increasing it did not change the results but significantly reduced the time step needed to run the simulation.

A.8. Viscous torque

The viscous torque model comes from the work of Ben Salam et al. (Ben Salem and Oesterle, 1998) and its implementation by Loth (2008).

$$Re_\omega = \frac{d_p^2 \omega_i \rho_f}{\mu} \tag{A.67}$$

$$C_v = 1 + \frac{5}{64\pi} Re_\omega^{0.6} \tag{A.68}$$

$$\boldsymbol{T^v} = -\pi C_v d_p^3 \omega_i \mu \tag{A.69}$$

We only use the low Reynolds value since the rotational Reynolds (Re_ω) in our case is sufficiently small. The fluid vorticity is neglected here since the bulk fluid velocity is assumed to be zero.

A.9. Induced torque

The induced torque applied to the particle is defined by the ANN regression. The regression is performed on data scaled by the drag coefficient of a single particle (see Eq. (1)), implying that it must be multiplied back by the drag coefficient of a single particle (Cd_0).

$$Ct = Cd_0(\text{Re}) Ct_{ANN}(\text{Re}, r^*, \theta) \tag{A.70}$$

$$\boldsymbol{n_{v,r}} = \boldsymbol{v_i} \times \boldsymbol{r} \tag{A.71}$$

$$\boldsymbol{T_{ij}^I} = \frac{1}{16} \rho_f \pi d_p^3 Ct \| \boldsymbol{v_i} \|^2 \frac{\boldsymbol{n_{v,r}}}{\| \boldsymbol{n_{v,r}} \|} \tag{A.72}$$

The resulting expression for torque correlation is too complex to detail here. For example, the resulting coefficient mapping as a function of the particle position relative to a reference particle for a given Reynold number of 10 is presented in Fig. A.21.

A.10. Relative velocity force models

The dataset with relative velocity described in Section 4.3 is used to define an ANN to capture the discrepancy between this new data set and the combination of the ANN force models and lubrication models. The same procedure presented in Section 2 is used to obtain a regression of the difference and compare the resulting force model with the simulation results. To improve the quality of the model, we supplement the data set with results of the ANN models of Section 2 without relative velocity, which helps isolate the effect of the relative velocity. To do so, each of the 2000 combinations of Re, $r^*, \theta, v_x^*, v_y^*$ are evaluated using the ANN model using the Re, r^*, θ and assuming $v_x^* = 0$ and $v_y^* = 0$. Using the same procedure presented in Section 2, we obtained an ANN of 6 layers with 25 neurons per layer.

A.10.1. Drag force

Parity plot of the ANN model for the drag combined with the lubrication force and the ANN model for the effect of the relative velocity on the induced drag force versus the Simulation data with relative velocity (see Fig. A.22).

A.10.2. Lift force

Parity plot of the ANN model for the lift force combined with the lubrication force and the ANN model for the effect of the relative velocity on the induced lift force versus the Simulation data with relative velocity (see Fig. A.23).

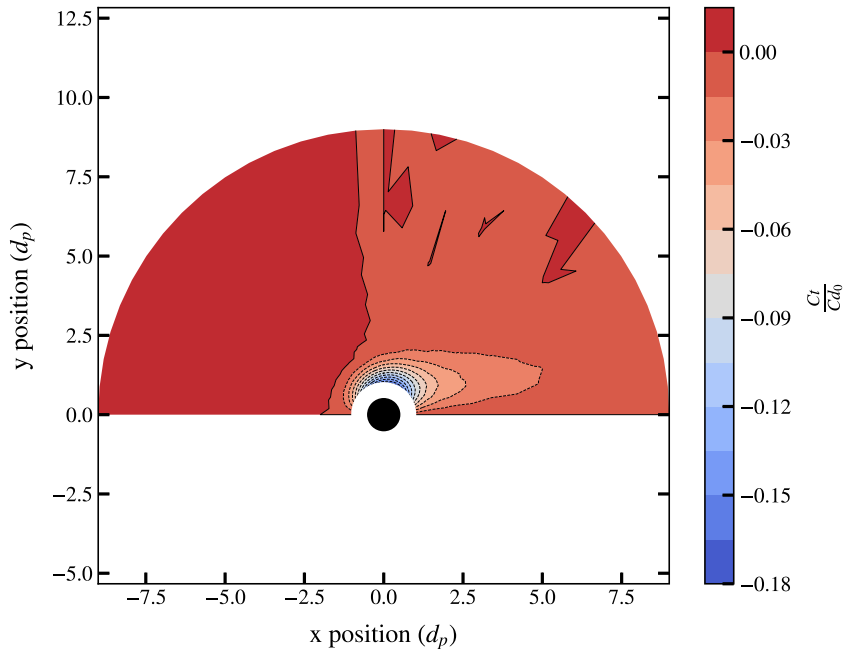

Fig. A.21. Torque coefficient correction factor at a Reynold number of 10. The velocity of the particle is assumed to be negative in x for in this figure.

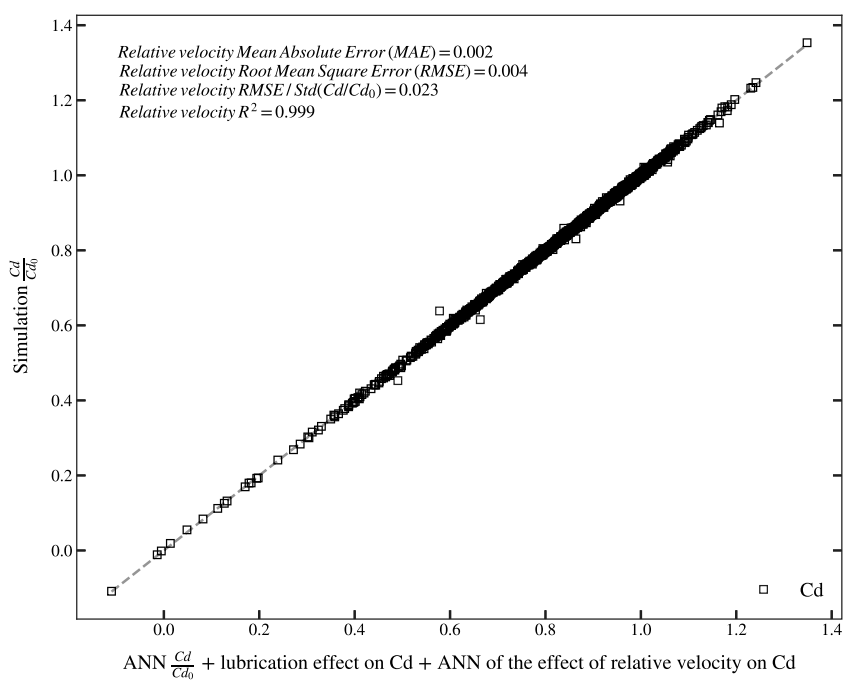

Fig. A.22. Parity plot of the ANN model for the drag combined with the lubrication force and the ANN model for the effect of the relative velocity versus the simulation data with relative velocity for the drag coefficient.

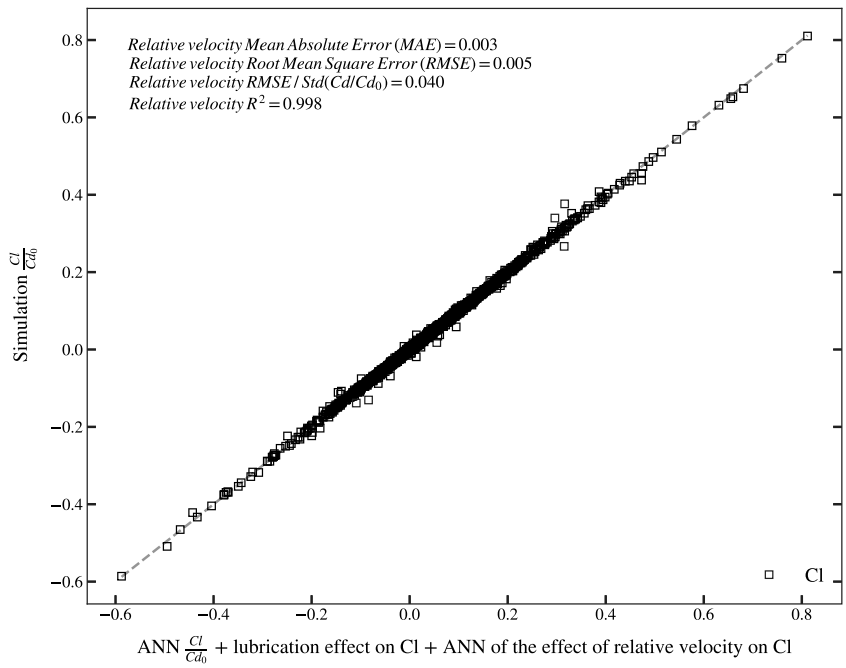

Fig. A.23. Parity plot of the ANN model for the lift combined with the lubrication force and the ANN model for the effect of the relative velocity versus the Simulation data with relative velocity for the lift coefficient.

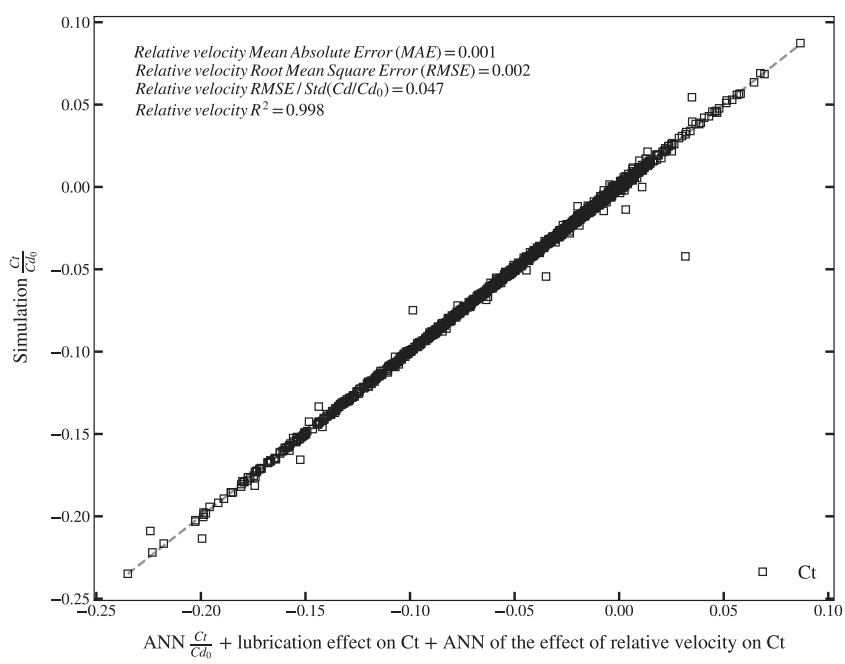

Fig. A.24. Parity plot of the ANN model for the induced torque combined with the lubrication force and the ANN model for the effect of the relative velocity versus the simulation data with relative velocity for the lift coefficient.

A.10.3. Induced torque

Parity plot of the ANN model for the drag combined with the lubrication force and the ANN model for the effect of the relative velocity on the induced torque versus the Simulation data with relative velocity (see Fig. A.24).

Appendix B. Fluid response time

Assuming the fluid flow response time (t) to reach a steady state after a perturbation of the flow is dependent on the following variable: $\| \boldsymbol{v} \|$, μ, ρ_f, d_p. The dimensional analysis leads to the following two dimensionless numbers if we choose the repeating variables to be μ, ρ_f, d_p.

$$\Pi_1 = \mathrm{Re} = \frac{\| \boldsymbol{v} \| \rho_f d_p}{\mu} \tag{B.1}$$

$$\Pi_2 = \frac{t\mu}{\rho_f d_p^2} = \frac{t}{t_f} \tag{B.2}$$

These two numbers are the Reynolds number and the dimensionless time associated with the flow response time. Isolating the characteristic fluid time from the dimensionless time we get the $t_f = \frac{\rho_f d_p^2}{\mu}$.

References

Abadi, M., Agarwal, A., Barham, P., Brevdo, E., Chen, Z., Citro, C., Corrado, G.S., Davis, A., Dean, J., Devin, M., Ghemawat, S., Goodfellow, I., Harp, A., Irving, G., Isard, M., Jia, Y., Jozefowicz, R., Kaiser, L., Kudlur, M., Levenberg, J., Mané, D., Monga, R., Moore, S., Murray, D., Olah, C., Schuster, M., Shlens, J., Steiner, B., Sutskever, I., Talwar, K., Tucker, P., Vanhoucke, V., Vasudevan, V., Viégas, F., Vinyals, O., Warden, P., Wattenberg, M., Wicke, M., Yu, Y., Zheng, X., 2015. TensorFlow: Large-scale machine learning on heterogeneous systems. URL: https://www.tensorflow.org/, Software available from tensorflow.org.

Akiki, G., Moore, W., Balachandar, S., 2017. Pairwise-interaction extended point-particle model for particle-laden flows. J. Comput. Phys. 351, 329–357.

Ardekani, A.M., Rangel, R.H., 2006. Unsteady motion of two solid spheres in Stokes flow. Phys. Fluids 18 (10), http://dx.doi.org/10.1063/1.2363351, arXiv:https://pubs.aip.org/aip/pof/article-pdf/doi/10.1063/1.2363351/14041205/103306_1_online.pdf, 103306.

Arndt, D., Bangerth, W., Feder, M., Fehling, M., Gassmöller, R., Heister, T., Heltai, L., Kronbichler, M., Maier, M., Munch, P., Pelteret, J.-P., Sticko, S., Turcksin, B., Wells, D., 2022. The `deal.II` library, version 9.4. J. Numer. Math. 30 (3), 231–246. http://dx.doi.org/10.1515/jnma-2022-0054, URL: https://dealii.org/deal94-preprint.pdf.

Barbeau, L., 2023. Pair of particles sedimentation ROM. GitHub repository, GitHub, URL: https://github.com/chaos-polymtl/particle_pair_sedimentation_dynamic.git.

Barbeau, L., Étienne, S., Béguin, C., Blais, B., 2022. Development of a high-order continuous Galerkin sharp-interface immersed boundary method and its application to incompressible flow problems. Comput. & Fluids 239, 105415. http://dx.doi.org/10.1016/j.compfluid.2022.105415, URL: https://www.sciencedirect.com/science/article/pii/S0045793022000780.

Barbeau, L., Golshan, S., Deng, J., Étienne, S., Béguin, C., Blais, B., 2024. High-order moving immersed boundary and its application to a resolved CFD-DEM model. Comput. & Fluids 268, 106094. http://dx.doi.org/10.1016/j.compfluid.2023.106094, URL: https://www.sciencedirect.com/science/article/pii/S0045793023003195.

Béguin, C., Pelletier, É., Étienne, S., 2016. Void fraction influence on added mass in a bubbly flow. Eur. J. Mech. B Fluids 56, 28–45. http://dx.doi.org/10.1016/j.euromechflu.2015.11.008, URL: https://www.sciencedirect.com/science/article/pii/S0997754615001272.

Ben Salem, M., Oesterle, B., 1998. A shear flow around a spinning sphere: Numerical study at moderate Reynolds numbers. Int. J. Multiph. Flow 24 (4), 563–585. http://dx.doi.org/10.1016/S0301-9322(97)00082-7, URL: https://www.sciencedirect.com/science/article/pii/S0301932297000827.

Bibeau, V., Barbeau, L., Boffito, D.C., Blais, B., 2023. Artificial neural network to predict the power number of agitated tanks fed by CFD simulations. Can. J. Chem. Eng. http://dx.doi.org/10.1002/cjce.24870, URL: https://onlinelibrary.wiley.com/doi/abs/10.1002/cjce.24870, arXiv:https://onlinelibrary.wiley.com/doi/pdf/10.1002/cjce.24870.

Blais, B., Barbeau, L., Bibeau, V., Gauvin, S., El Geitani, T., Golshan, S., Kamble, R., Mikahori, G., Chaouki, J., 2020. Lethe: An open-source parallel high-order adaptative CFD solver for incompressible flows. SoftwareX 12, 100579.

Candelier, F., Mehaddi, R., Mehlig, B., Magnaudet, J., 2023. Second-order inertial forces and torques on a sphere in a viscous steady linear flow. J. Fluid Mech. 954, A25.

Chen, R., Lu, Y., 1999. The flow characteristics of an interactive particle at low Reynolds numbers. Int. J. Multiph. Flow 25 (8), 1645–1655.

Chen, R., Wu, J., 2000. The flow characteristics between two interactive spheres. Chem. Eng. Sci. 55 (6), 1143–1158.

Cheng, Z., Wachs, A., 2023. Physics-informed neural network for modelling force and torque fluctuations in a random array of bidisperse spheres. arXiv preprint arXiv:2305.03326.

Clift, R., Grace, J.R., Weber, M.E., 2005. Bubbles, Drops, and Particles. Courier Corporation.

Cooley, M., O'neill, M., 1969. On the slow motion generated in a viscous fluid by the approach of a sphere to a plane wall or stationary sphere. Mathematika 16 (1), 37–49.

Cundall, P.A., Strack, O.D., 1979. A discrete numerical model for granular assemblies. Geotechnique 29 (1), 47–65.

Daunais, C.-A., Barbeau, L., Blais, B., 2023. An extensive study of shear thinning flow around a spherical particle for power-law and Carreau fluids. J. Non-Newton. Fluid Mech. 311, 104951.

Di Felice, R., 1994. The voidage function for fluid-particle interaction systems. Int. J. Multiph. Flow 20 (1), 153–159.

Dorgan, A., Loth, E., 2007. Efficient calculation of the history force at finite Reynolds numbers. Int. J. Multiph. Flow 33 (8), 833–848. http://dx.doi.org/10.1016/j.ijmultiphaseflow.2007.02.005, URL: https://www.sciencedirect.com/science/article/pii/S0301932207000304.

Ergun, S., 1952. Fluid flow through packed columns. Chem. Eng. Prog. 48 (2), 89–94.

Eveson, G., Hall, E., Ward, S., 1959. Interaction between two equal-sized equal-settling spheres moving through a viscous liquid. Br. J. Appl. Phys. 10 (1), 43.

Faxen, H., 1923. Die bewegung einer starren kugel langs der achse eines mit zaher flussigkeit gefullten rohres. Ark. Matemetik Astron. och Fysik 17, 1–28.

Ferreira, V.O., Geitani, T.E., Silva, D., Blais, B., Lopes, G.C., 2023. In-depth validation of unresolved CFD-dem simulations of liquid fluidized beds. Powder Technol. 426, 118652. http://dx.doi.org/10.1016/j.powtec.2023.118652, URL: https://www.sciencedirect.com/science/article/pii/S0032591023004369.

Gatignol, R., 1983. The faxen formulae for a rigid particle in an unsteady non-uniform stokes flow. J. Mec. Theor. Appl. (ISSN: 0750-7240) 2 (2), 143–160, FRA; DA., ABS. FRE; BIBL. 30 REF.

Géron, A., 2022. Hands-On Machine Learning with Scikit-Learn, Keras, and TensorFlow. O'Reilly Media, Inc..

Glorot, X., Bengio, Y., 2010. Understanding the difficulty of training deep feedforward neural networks. In: Proceedings of the Thirteenth International Conference on Artificial Intelligence and Statistics. JMLR Workshop and Conference Proceedings, pp. 249–256.

Golshan, S., Munch, P., Gassmöller, R., Kronbichler, M., Blais, B., 2023. Lethe-DEM: An open-source parallel discrete element solver with load balancing. Comput. Part. Mech. 10 (1), 77–96.

Golshan, S., Sotudeh-Gharebagh, R., Zarghami, R., Mostoufi, N., Blais, B., Kuipers, J., 2020. Review and implementation of CFD-DEM applied to chemical process systems. Chem. Eng. Sci. 221, 115646. http://dx.doi.org/10.1016/j.ces.2020.115646, URL: https://www.sciencedirect.com/science/article/pii/S0009250920301780.

Happel, J., Brenner, H., 1983. Low Reynolds Number Hydrodynamics: with Special Applications to Particulate Media, vol. 1, Springer Science & Business Media.

Jin, H., Wang, H., Wu, Z., Ren, Z., Ou, Z., 2019. Numerical investigation on drag coefficient and flow characteristics of two biomass spherical particles in supercritical water. Renew. Energy 138, 11–17.

Kelly, D.W., De SR Gago, J., Zienkiewicz, O.C., Babuska, I., 1983. A posteriori error analysis and adaptive processes in the finite element method: Part I—error analysis. Internat. J. Numer. Methods Engrg. 19 (11), 1593–1619.

Kim, I., Elghobashi, S., Sirignano, W.A., 1998. On the equation for spherical-particle motion: effect of Reynolds and acceleration numbers. J. Fluid Mech. 367, 221–253. http://dx.doi.org/10.1017/S0022112098001657.

Kriebitzsch, S., Van der Hoef, M., Kuipers, J., 2013. Fully resolved simulation of a gas-fluidized bed: a critical test of DEM models. Chem. Eng. Sci. 91, 1–4.

Li, T., Wang, L., Rogers, W., Zhou, G., Ge, W., 2017. An approach for drag correction based on the local heterogeneity for gas–solid flows. AIChE J. 63 (4), 1203–1212. http://dx.doi.org/10.1002/aic.15507, URL: https://aiche.onlinelibrary.wiley.com/doi/abs/10.1002/aic.15507, arXiv:https://aiche.onlinelibrary.wiley.com/doi/pdf/10.1002/aic.15507.

Liang, S.-C., Hong, T., Fan, L.-S., 1996. Effects of particle arrangements on the drag force of a particle in the intermediate flow regime. Int. J. Multiph. Flow 22 (2), 285–306.

Loth, E., 2008. Lift of a spherical particle subject to vorticity and/or spin. AIAA J. 46 (4), 801–809. http://dx.doi.org/10.2514/1.29159.

Marchelli, F., Di Felice, R., 2023. An experimental assessment of fluid-solid drag models based on the pressure drop in bidisperse fixed beds. Int. J. Multiph. Flow 104513. http://dx.doi.org/10.1016/j.ijmultiphaseflow.2023.104513, URL: https://www.sciencedirect.com/science/article/pii/S0301932223001349.

McKay, M.D., Beckman, R.J., Conover, W.J., 2000. A comparison of three methods for selecting values of input variables in the analysis of output from a computer code. Technometrics 42 (1), 55–61.

Mei, R., Adrian, R.J., 1992. Flow past a sphere with an oscillation in the free-stream velocity and unsteady drag at finite Reynolds number. J. Fluid Mech. 237, 323–341.

Nijssen, T.M., Kuipers, H.A., van der Stel, J., Adema, A.T., Buist, K.A., 2020. Complete liquid-solid momentum coupling for unresolved CFD-DEM simulations. Int. J. Multiph. Flow 132, 103425.

O'Neill, M.E., Majumdar, S.R., 1970. Asymmetrical slow viscous fluid motions caused by the translation or rotation of two spheres. Part II: Asymptotic forms of the solutions when the minimum clearance between the spheres approaches zero. Z. Angew. Math. Phys. 21, 180–187.

Parmar, M., Annamalai, S., Balachandar, S., Prosperetti, A., 2018. Differential formulation of the viscous history force on a particle for efficient and accurate computation. J. Fluid Mech. 844, 970–993. http://dx.doi.org/10.1017/jfm.2018.217.

Prahl, L., Hölzer, A., Arlov, D., Revstedt, J., Sommerfeld, M., Fuchs, L., 2007. On the interaction between two fixed spherical particles. Int. J. Multiph. Flow 33 (7), 707–725. http://dx.doi.org/10.1016/j.ijmultiphaseflow.2007.02.001, URL: https://www.sciencedirect.com/science/article/pii/S0301932207000249.

Rong, L., Dong, K., Yu, A., 2013. Lattice-Boltzmann simulation of fluid flow through packed beds of uniform spheres: Effect of porosity. Chem. Eng. Sci. 99, 44–58. http://dx.doi.org/10.1016/j.ces.2013.05.036, URL: https://www.sciencedirect.com/science/article/pii/S0009250913003679.

Seyed-Ahmadi, A., Wachs, A., 2020. Microstructure-informed probability-driven point-particle model for hydrodynamic forces and torques in particle-laden flows. J. Fluid Mech. 900, A21.

Simeonov, J.A., Calantoni, J., 2012. Modeling mechanical contact and lubrication in direct numerical simulations of colliding particles. Int. J. Multiph. Flow 46, 38–53.

Smoluchowski, M., 1911. Über die Wechselwirkung von Kugeln die sich in einer zähen Flüssigkeit bewegen. Akad. Umiejętności.

Su, M., Zhao, H., 2017. Modifying the inter-phase drag via solid volume fraction gradient for CFD simulation of fast fluidized beds. AIChE J. 63 (7), 2588–2598.

ten Cate, A., Nieuwstad, C.H., Derksen, J.J., Van den Akker, H.E.A., 2002. Particle imaging velocimetry experiments and lattice-Boltzmann simulations on a single sphere settling under gravity. Phys. Fluids 14 (11), 4012–4025. http://dx.doi.org/10.1063/1.1512918, URL: http://aip.scitation.org/doi/10.1063/1.1512918.

van Wachem, B., Elmestikawy, H., Chéron, V., 2024. Microstructure-based prediction of hydrodynamic forces in stationary particle assemblies. Int. J. Multiph. Flow 175, 104815. http://dx.doi.org/10.1016/j.ijmultiphaseflow.2024.104815, URL: https://www.sciencedirect.com/science/article/pii/S0301932224000958.

Zhu, C., Liang, S., Fan, L.S., 1994. Particle wake effects on the drag force of an interactive particle. Int. J. Multiph. Flow 20 (1), 117–129.

Zoghlami, S., Béguin, C., Etienne, S., Scott, D., Bornard, L., 2019. The role of added mass in the dispersion of bubble clouds. IOP Conf. Ser. Earth Environ. Sci. 240 (6), 062050. http://dx.doi.org/10.1088/1755-1315/240/6/062050.